



Formation of Wind Gusts in an Extratropical Cyclone in Light of Doppler Lidar Observations and Large-Eddy Simulations

Florian Pantillon, Bianca Adler, Ulrich Corsmeier, Peter Knippertz, Andreas Wieser, Akio Hansen

► To cite this version:

Florian Pantillon, Bianca Adler, Ulrich Corsmeier, Peter Knippertz, Andreas Wieser, et al.. Formation of Wind Gusts in an Extratropical Cyclone in Light of Doppler Lidar Observations and Large-Eddy Simulations. *Monthly Weather Review*, 2020, 148 (1), pp.353-375. 10.1175/MWR-D-19-0241.1 . hal-02333535

HAL Id: hal-02333535

<https://hal.science/hal-02333535>

Submitted on 10 Nov 2020

HAL is a multi-disciplinary open access archive for the deposit and dissemination of scientific research documents, whether they are published or not. The documents may come from teaching and research institutions in France or abroad, or from public or private research centers.

L'archive ouverte pluridisciplinaire **HAL**, est destinée au dépôt et à la diffusion de documents scientifiques de niveau recherche, publiés ou non, émanant des établissements d'enseignement et de recherche français ou étrangers, des laboratoires publics ou privés.



Formation of Wind Gusts in an Extratropical Cyclone in Light of Doppler Lidar Observations and Large-Eddy Simulations

FLORIAN PANTILLON

*Institute of Meteorology and Climate Research, Karlsruhe Institute of Technology, Karlsruhe, Germany, and
Laboratoire d'Aérodynamique, Université de Toulouse/CNRS/UPS, Toulouse, France*

BIANCA ADLER, ULRICH CORSMEIER, PETER KNIPPERTZ, AND ANDREAS WIESER

Institute of Meteorology and Climate Research, Karlsruhe Institute of Technology, Karlsruhe, Germany

AKIO HANSEN

Meteorological Institute, Universität Hamburg, Hamburg, Germany

(Manuscript received 18 July 2019, in final form 10 October 2019)


ABSTRACT


Damaging gusts in windstorms are represented by crude subgrid-scale parameterizations in today's weather and climate models. This limitation motivated the Wind and Storms Experiment (WASTEX) in winter 2016–17 in the Upper Rhine Valley over southwestern Germany. Gusts recorded at an instrumented tower during the passage of extratropical cyclone “Thomas” on 23 February 2017 are investigated based on measurements of radial wind with ≈ 70 -m along-beam spacing from a fast-scanning Doppler lidar and realistic large-eddy simulations with grid spacings down to 78 m using the Icosahedral Nonhydrostatic model. Four wind peaks occur due to the storm onset, the cold front, a precipitation line, and isolated showers. The first peak is related to a sudden drop in dewpoint and results from the downward mixing of a low-level jet and a dry layer within the warm sector characterized by extremely high temperatures for the season. While operational convection-permitting forecasts poorly predict the storm onset overall, a successful ensemble member highlights the role of upstream orography. Lidar observations reveal the presence of long-lasting wind structures that result from a combination of convection- and shear-driven instability. Large-eddy simulations contain structures elongated in the wind direction that are qualitatively similar but too coarse compared to the observed ones. Their size is found to exceed the effective model resolution by one order of magnitude due to their elongation. These results emphasize the need for subkilometer-scale measuring and modeling systems to improve the representation of gusts in windstorms.

1. Introduction

Intense extratropical cyclones belong to the main meteorological hazards in midlatitudes due to the associated

windstorms and they strongly affect regions located downstream of the North Atlantic storm track (Lamb and Frydendahl 1991). Therefore, European windstorms have been widely studied in both academia and industry due to large insurance losses associated with extreme events (e.g., Pinto et al. 2019). Overall, the dynamics and life cycle of extratropical cyclones are well understood at the synoptic scale thanks to a century of research on the topic [see Schultz et al. (2018) for a historical review]. However, the contribution to the strongest winds from mesoscale airflows is still debated (Hewson and Neu 2015), in particular from sting jets (Clark and Gray 2018), whereas at smaller scales, convection (e.g., embedded in the cold front) can bring down high momentum to

 Denotes content that is immediately available upon publication as open access.

 Supplemental information related to this paper is available at the Journals Online website: <https://doi.org/10.1175/MWR-D-19-0241.s1>.

Corresponding author: Florian Pantillon, florian.pantillon@aero.obs-mip.fr

DOI: 10.1175/MWR-D-19-0241.1

© 2019 American Meteorological Society. For information regarding reuse of this content and general copyright information, consult the AMS Copyright Policy (www.ametsoc.org/PUBSReuseLicenses).

the surface and thus be responsible for the formation of devastating gusts (Ludwig et al. 2015).

The damaging impact of windstorms on infrastructure is mainly due to gusts (i.e., short but intense wind peaks typically measured over periods of 3 s) (Klawe and Ulbrich 2003). Sharp increases in wind intensity are also an issue for the wind energy sector due to the threat they represent to turbines (Zhou et al. 2018). In weather and climate models, gusts are represented by parameterization schemes due to their subgrid-scale nature, even at convection-permitting resolution with grid spacings of $O(1)$ km. These schemes can be based on empirical (Panofsky et al. 1977) or physical assumptions (Brasseur 2001) to represent the complex formation of gusts in a simplified way. Gusts are also difficult to capture with surface observation networks due to their local scale (Friederichs et al. 2009). The gust footprint of windstorms is often obtained by combined statistical-dynamical downscaling of global or regional models corrected with observations (Della-Marta et al. 2009; Roberts et al. 2014).

Emerging technologies have brought new opportunities to alleviate these limitations in the understanding of gust formation. On the observational side, Doppler lidar instruments have become widely available in recent years. They offer solutions to measure gusts beyond heights usually attained by instrumented towers or when those are not available (Suomi et al. 2017). They also allow sampling the wind over an area rather than at a single point as with traditional systems (Suomi and Vihma 2018). Three decades after early work by Neiman et al. (1988), who found propagating wind gusts in Doppler lidar measurements of a downslope windstorm, these instruments are increasingly popular in the wind energy sector to anticipate quick variations in wind speed (Bos et al. 2016). On the modeling side, realistic large-eddy simulations are now possible for case studies. They can be used for the dynamical downscaling of numerical weather predictions and provide a framework to forecast turbulence at the 10–100-m scale (Muñoz Esparza et al. 2018). The increase in computational power further allows running large-eddy simulations for a day over a domain extending over several 100 km, thus encompassing synoptic-scale systems (Heinze et al. 2017).

These new opportunities are exploited here to investigate what physical mechanisms are responsible for the formation of gusts during the passage of an extratropical cyclone and how well they are represented by different types of models. Several cases were sampled with a Doppler lidar during the Wind and Storms Experiment (WASTEX) that took place in winter 2016–17 on a former waste deposit topping at 50-m height and

located in the Upper Rhine Valley near Karlsruhe in southwestern Germany (Pantillon et al. 2018b). Doppler lidar measurements are challenging in extratropical cyclones due to the low aerosol load, which hinders observations after the passage of fronts. This was the case during the extreme windstorm “Egon” on 12–13 January 2017, which involved an unprecedented sting jet over continental Europe (Eisenstein et al. 2019) but could not be sampled satisfactorily. Data quality was much better during other WASTEX case studies including the intense windstorm “Thomas” on 23 February 2017, which is the focus of the paper. Data from three additional windstorms that were well sampled by Doppler lidar are also used for comparison: “Stefan” on 22 February, “Udo” on 27 February, and “Wilfried” on 2 March (Pantillon et al. 2018b). Finally, large-eddy simulations are run with grid spacings approximately matching the spacing of Doppler lidar measurements. These high-resolution data are combined with observations from an instrumented tower, a C-band radar, and a surface station as well as deterministic and ensemble predictions at convection-permitting resolution to investigate the multiscale contributions to gusts and their predictability.

Section 2 presents the observational data collected during the WASTEX campaign, the available operational forecasts, and the large-eddy simulations. Section 3 gives a general overview of synoptic dynamics of the case study. Section 4 describes the local evolution at the WASTEX site based on observations and its representation in models. Section 5 analyses the structure of boundary layer winds in Doppler lidar measurements and large-eddy simulations. Finally, section 6 summarizes and discusses the results to conclude the paper.

2. Data and methods

a. Observations

The key instrument of the WASTEX field campaign was the Lockheed Martin WindTracer HYB, a scanning Doppler lidar of the KITcube observation platform (Kalthoff et al. 2013). The instrument measured boundary layer winds by performing range–height–indicator scans between 0° and 15° elevation every 10 s in the main flow direction with an along-beam spacing of ≈ 70 m. The azimuthal orientation was automatically readjusted every hour to follow wind turning but changed only little due to channeling in the Upper Rhine Valley. The measurement range, which depends on the aerosol load of the boundary layer, typically reached a few km during WASTEX. The lidar does not exhibit systematic biases and uncorrelated noise usually remains within 0.15 m s^{-1} in the high signal-to-noise range (Träumner et al. 2011). The data are filtered based on the signal-to-noise ratio

and interpolated on a Cartesian grid. The radial velocity is corrected for the elevation angle by assuming that the mean wind is essentially horizontal and its low-frequency vertical component negligible.

Doppler lidar measurements are complemented with observations from a 200-m-high instrumented meteorological tower (Kohler et al. 2018) and a C-Band Doppler radar both located about 10 km northeastward at Campus North of the Karlsruhe Institute of Technology (KIT). Combining tower records from different levels allows computing the bulk Richardson number Ri as the ratio of squared Brunt–Väisälä frequency N and vertical wind shear in a layer:

$$Ri = \frac{N^2}{(\Delta U / \Delta z)^2} = \frac{(g/T)(\Delta \theta / \Delta z)}{(\Delta U / \Delta z)^2}, \quad (1)$$

where g is the gravity; T is the layer-averaged temperature; and ΔU , $\Delta \theta$, and Δz are the differences in wind, potential temperature, and height between two levels, respectively. Tower measurements are complemented with surface observations from the Deutscher Wetterdienst (DWD) surface network, in particular from a nearby station located in Rheinstetten about 5 km southward of the Doppler lidar. See Fig. 1 for locations and Pantillon et al. (2018b) for more details about the instrumentation during the WASTEX field campaign.

b. Operational forecasts

Regional analyses and forecasts over Germany are produced operationally every 3 h by the DWD using the model developed by the Consortium for Small-Scale Modeling (COSMO-DE; Baldauf et al. 2011). They are run on a rotated grid with 50 vertical levels and 2.8-km horizontal spacing, which allows explicit representation of moist convection. While convective gusts are also explicitly represented, turbulent gusts are parameterized using a subgrid-scale scheme based on the resolved 10-m wind speed and the friction velocity u^* scaled by empirical factors (Schulz 2008). In addition to the COSMO-DE deterministic forecast, the COSMO-DE-EPS ensemble prediction system is computed on the same grid with 20 members. As of February 2017, the members were downscaled from four global models combined with five sets of physical perturbations (Peralta et al. 2012). During windstorms, this model design often results in four groups of similar forecasts where the uncertainty is inherited mostly from the global models (Pantillon et al. 2018a). Furthermore, COSMO-DE-EPS exhibits systematic errors in winds and gusts, and lacks calibration. Following Pantillon et al. (2018a), statistical postprocessing is applied here to winds and gusts using ensemble

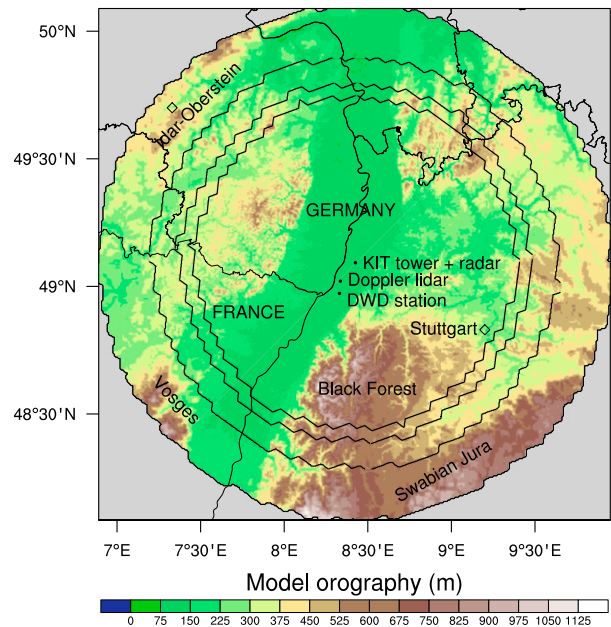


FIG. 1. Model orography in ICON large-eddy simulations. Concentric circles show the boundaries of nested domains with 623-, 311-, 156-, and 78-m grid spacing. Dots and diamonds show the location of instruments used during the WASTEX field campaign and of operational radiosoundings, respectively. Relevant mountain ranges are labeled.

model output statistics trained with six winters of forecast and observation data from the 2011–16 period.

c. Model simulations

Realistic large-eddy simulations are run with the Icosahedral Nonhydrostatic (ICON) modeling framework (Zängl et al. 2015; Dipankar et al. 2015). Based on the setup of Heinze et al. (2017) modified as in Marke et al. (2018), the model is run with one-way nesting on four nested domains with 623-, 311-, 156-, and 78-m grid spacing. In the vertical, the model has 150 full levels up to 21 km and the spacing is roughly 20 m near surface and stretches with increasing height. Turbulence is parameterized by a three-dimensional, diagnostic Smagorinsky scheme with modifications from Lilly (1962) to include thermal stratification effects. The domain is centered on the WASTEX site and encompasses the northern part of the Upper Rhine Valley (Fig. 1). Note the circular shape of the domain allowed by the triangular cell geometry of ICON. The innermost nest includes the northern Black Forest, while the outermost nest extends farther southward to parts of the Swabian Jura and Vosges Mountains. The terrain resolution increases with model resolution, thus the orography is finer in inner than in outer nested domains. Initial and lateral boundary conditions are taken from hourly

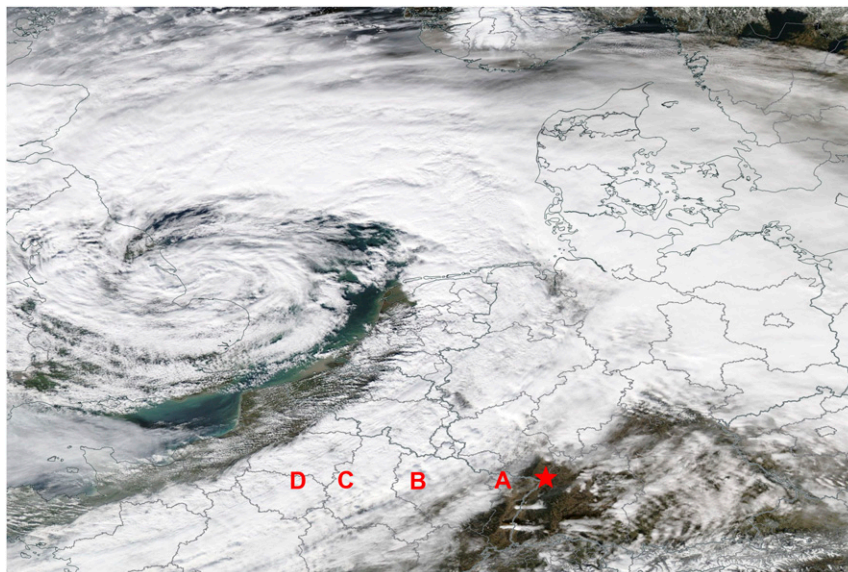


FIG. 2. Satellite imagery of storm Thomas at 1225 UTC 23 Feb 2017: Moderate Resolution Imaging Spectroradiometer (MODIS) corrected reflectance from the *Aqua* satellite. The red star indicates the location of the WASTEX site and labels “A,” “B,” “C,” and “D” its cyclone-relative position at 1330, 1530, 1700, and 1800 UTC.

COSMO-DE analyses from 0000 to 2400 UTC 23 February 2017, which share the horizontal and vertical grid spacing of COSMO-DE forecasts described above. Further details of the model setup can be found in Heinze et al. (2017) and Marke et al. (2018).

3. Synoptic overview

On 22 February 2017 low pressure system Thomas¹ developed over the North Atlantic during a secondary cyclogenesis then intensified explosively before moving toward continental Europe. Satellite imagery around noon on 23 February shows that the cyclone center was located over the North Sea, while its cold front had reached land and was approximately aligned with the French, Belgian, and Dutch coasts (Fig. 2). The WASTEX site was situated in a cloud-free area within the warm sector at that time (red star). The synoptic situation is well depicted by the COSMO-DE analysis at 1200 UTC (Fig. 3). The cold front, defined by the gradient in equivalent potential temperature, was preceded by strong low-level winds corresponding to the warm conveyor belt jet with a maximum over the Netherlands (Figs. 3a,b). Strong low-level winds were also surrounding the northern side of the Alps in a region marked by an

area of very warm and dry air (Figs. 3b–d). This region is of particular interest here, because it includes the Upper Rhine Valley and thus the WASTEX site (black star). Interestingly, the region does not stand out from the rest of the warm sector in maps of equivalent potential temperature, as high temperature and low humidity compensate each other (Fig. 3a). The layer of very warm and dry air extends southwestward well beyond the COSMO-DE domain (not shown). Its origin is possibly related to Saharan air advected from a stationary cyclone on the lee side of the Atlas Mountains, which resulted in an extreme dust outbreak over the Iberian Peninsula on 21–23 February (Rodríguez-Navarro et al. 2018).

4. Local conditions

a. Observed time evolution

Observations from the DWD surface station in Rheinstetten and from different heights of the 200-m KIT tower provide detailed insights into the lower boundary layer during the passage of Thomas on 23 February at the WASTEX site (Fig. 4), while Doppler lidar measurements processed over 10-min time intervals summarize the evolution of local wind conditions (Fig. 5).

Station and tower time series generally show a similar evolution during the course of the day but also emphasize local differences. Average wind speed and gusts agree on a windy night followed by a calmer morning, a stormy

¹ As named by the Free University of Berlin, while baptized Doris by Met Éireann and the Met Office.

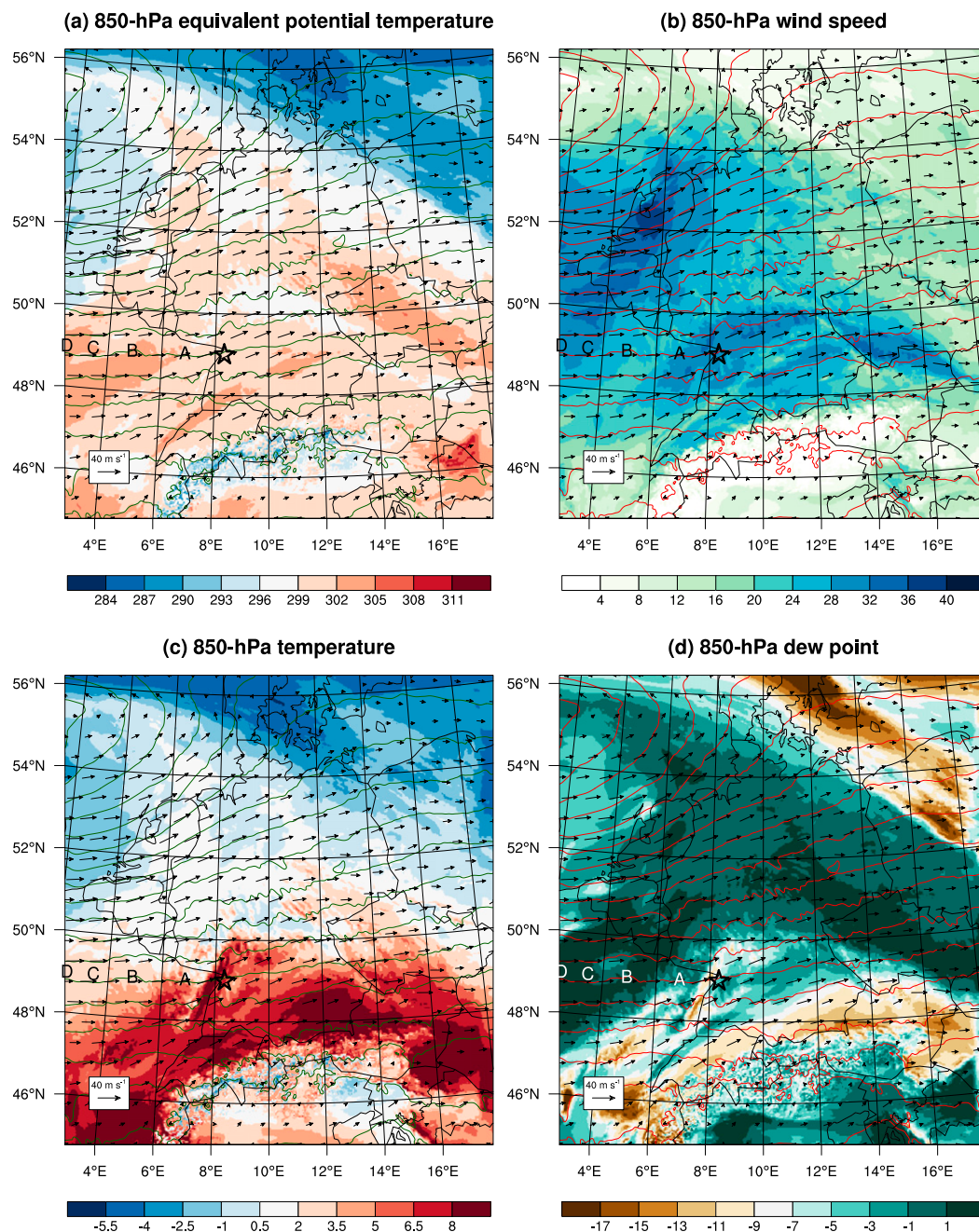


FIG. 3. Synoptic structure of storm Thomas over Germany and neighboring countries at 1200 UTC 23 Feb 2017 in the COSMO-DE analysis: (a) 850-hPa equivalent potential temperature (in K), (b) wind speed (in m s^{-1}), (c) temperature (in $^{\circ}\text{C}$), and (d) dewpoint (in $^{\circ}\text{C}$). Contours show the 850-hPa geopotential height every 200 m, arrows depict the 850-hPa wind, and the star indicates the location of the WASTEX site and labels “A,” “B,” “C,” and “D” its cyclone-relative position at 1330, 1530, 1700, and 1800 UTC.

afternoon, and a windy evening (Figs. 4a,b). Four major peaks are recorded around 1330, 1530, 1700, and 1800 UTC (labels A, B, C, and D). Although their exact timing and relative amplitude exhibit some variability, these peaks are present at all levels and both sites. In contrast, additional strong peaks are found later on but vary more

between DWD surface station (black curves) and KIT tower (red, blue, and green curves). Similarly, a weaker peak is recorded after sunrise near 0630 UTC at all tower levels but is not clearly seen at the surface station. Note that the higher wind speed at 10 m AGL compared to 30 m AGL may appear surprising but is explained by

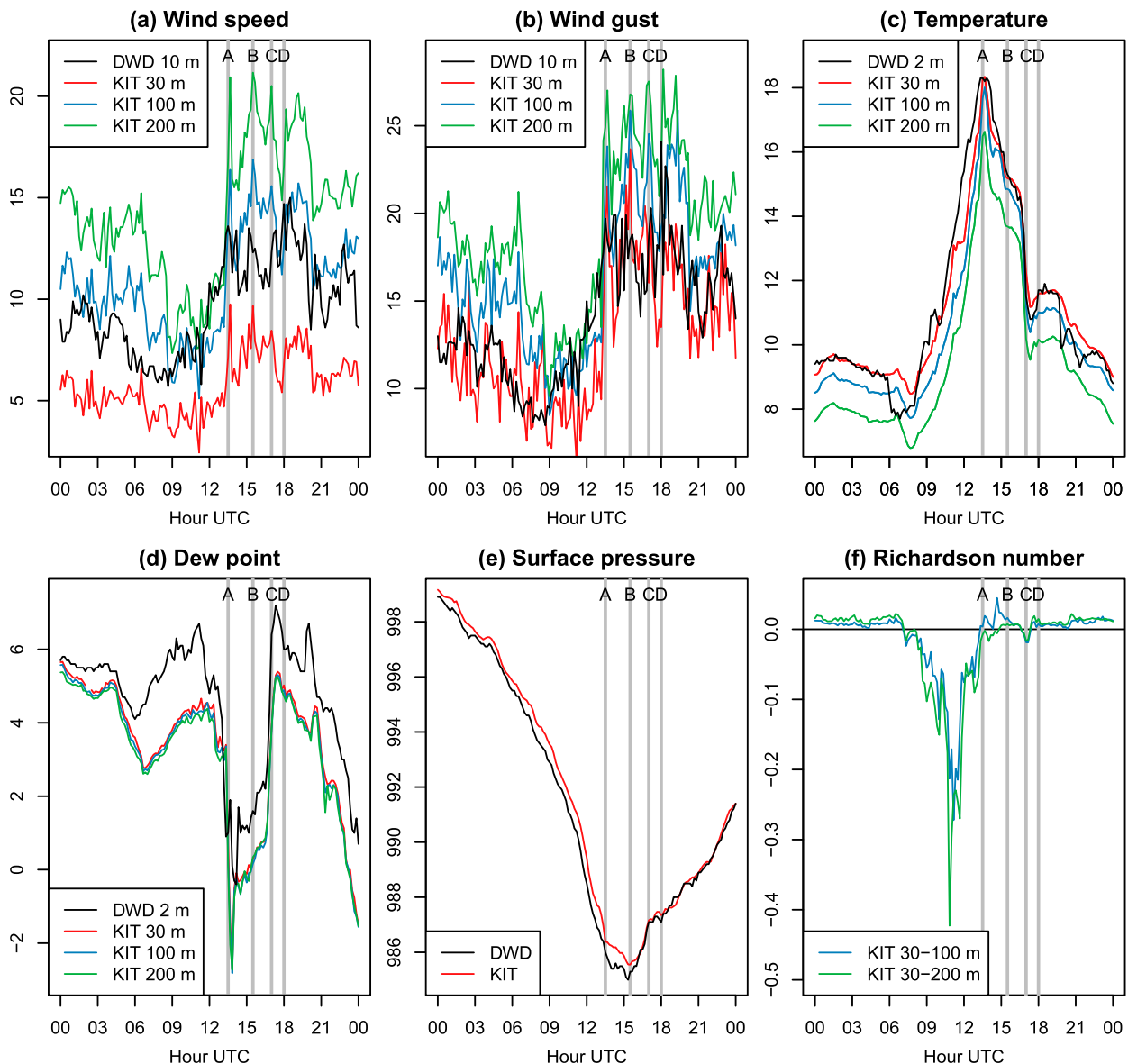


FIG. 4. Time series of 10-min observations at the DWD surface station (black curves) and at different levels of the KIT tower (color curves) on 23 Feb 2017: (a),(b) wind speed and gusts (in m s^{-1}); (c),(d) temperature and dewpoint (in $^{\circ}\text{C}$); (e) surface pressure (in hPa) and (f) bulk Richardson number. Labels “A,” “B,” “C,” and “D” mark the time of wind peaks at 1330, 1530, 1700, and 1800 UTC.

the lower roughness length at the DWD surface station situated over open fields compared to the KIT tower located in a forest. For wind gusts, this difference is partly compensated by the 1-s interval used at the KIT tower instead of the standard 3-s interval used at the DWD station. These factors affect the measured values but not their evolution.

Corroborating station and tower observations, moderate winds are measured by Doppler lidar during the night (Fig. 5a). They show a regular increase in intensity with height and suggest the presence of remnants of storm Stefan, which preceded Thomas on 22 February.

After the sunrise peak near 0630 UTC, the wind speed weakens and remains low for the morning hours below 400 m AGL. However, it strengthens aloft to form a low-level jet with a sharp vertical gradient. Later only, near 1130 UTC, strong winds start mixing downward to reach the surface and the wind speed increases across the boundary layer, remaining strong during the afternoon. As in time series of station and tower observations (Figs. 4a,b) the wind measured by Doppler lidar exhibits two broad peaks around 1330 and 1530 UTC then two sharper peaks near 1700 and 1800 UTC (labels A, B, C, and D in Fig. 5a), before weakening slowly in the evening.

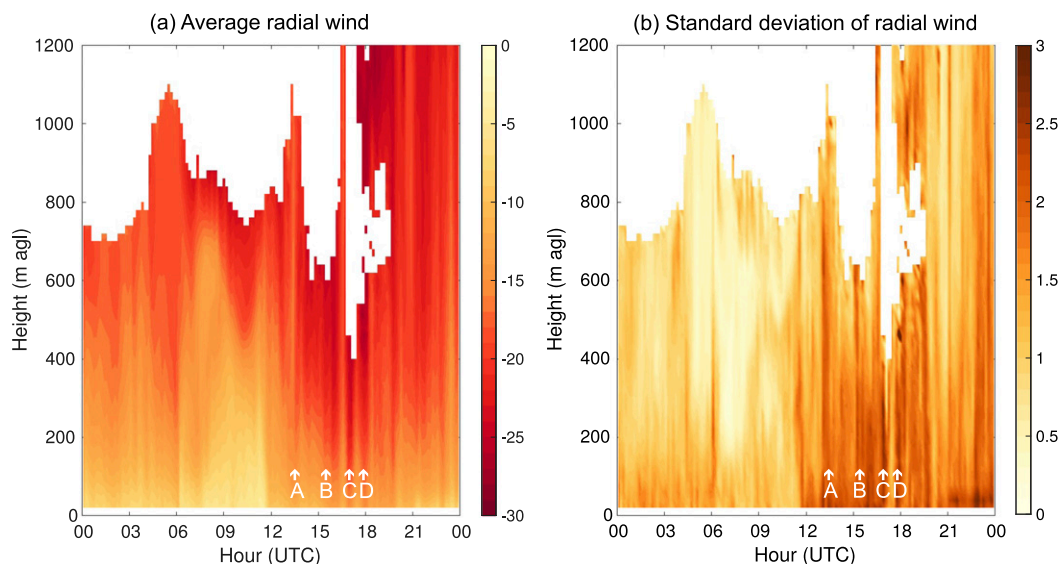


FIG. 5. Time–height plots of (a) the average and (b) the standard deviation of radial wind over 10-min periods as measured by Doppler lidar on 23 Feb 2017 (in m s^{-1}). The data in elevation–range coordinates is first interpolated onto a regular grid every 20 m AGL, then the median is taken at each height over all horizontal distances with at least 5% of valid data. Following the mean wind direction, the azimuth angle remained constant at 230° until 2100 UTC, when it turned clockwise to 246° . Labels “A,” “B,” “C,” and “D” mark the time of wind peaks at 1330, 1530, 1700, and 1800 UTC as in Fig. 4.

This evolution can also be seen in the standard deviation of lidar winds (Fig. 5b), which is computed at each height over 10-min intervals and over the horizontal range and is here taken as a proxy for turbulent kinetic energy (TKE). In contrast to the average radial wind, TKE generally decreases with height and maximizes due to friction in the surface layer. Similar to wind speed, TKE in this layer reveals four periods with first moderate values during the night that then diminish in the morning followed by highest values in the afternoon that remain elevated in the evening. Note that the increased TKE after 2100 UTC might be due to different roughness elements along the lidar line of sight, because the azimuth angle was rotated from 230° to 246° following the mean wind direction at that time. Above the surface layer, high TKE highlights the transition periods near 0630 and 1130 UTC that mark the beginning and end of the morning calm winds. Several peaks indicating strong turbulence across the boundary layer are found later on (labels A, B, C, and D in Fig. 5b) and match the peaks in time series and Doppler winds found previously.

The maximum height attained by lidar observations in Fig. 5 is related to the presence of backscatter particles along the instrument line of sight and thus provides further information about local conditions. Prior to 1700 UTC (C), a quick increase in maximum height above 1200 m indicates enhanced backscattering of the lidar beam likely due to a descending cloud base or falling droplets during the onset of precipitation.

This increase in maximum height is followed by a sharp decrease down to 400 m, which suggests the washout of aerosols by precipitation possibly combined with the subsidence of aerosol-free air. Accordingly, the passage of a precipitation line over the lidar site is observed by the KIT radar from 1630 to 1700 UTC (cross in Fig. 6a). A clear dipole in the Doppler pattern of radial velocities emphasizes the approximate alignment of the precipitation line with the wind direction at 1000 m AGL (Fig. 6b). Thanks to this alignment and to the passage over the radar instrument, the radial velocity approximately matches the wind speed, although it could be affected by falling hydrometeors. The wind speed is estimated to be $25\text{--}30 \text{ m s}^{-1}$, which is consistent with Doppler lidar measurements taken at that height (Fig. 5a). This illustrates how both instruments can complement each other in some situations. However, the availability of Doppler radar winds is restricted to a short period of time here, because precipitation was absent earlier and only appeared in isolated showers later on.

Similar to the wind records, the station and tower time series of temperature also show local differences but a similar evolution overall (Fig. 4c). A short cooling at sunrise is followed by a continuous warming until 1330 UTC (A), when the 2-m temperature reaches an unprecedented high of 18.4°C . This record is the warmest during wintertime (December–February) for the available period 2009–18 in Rheinstetten.

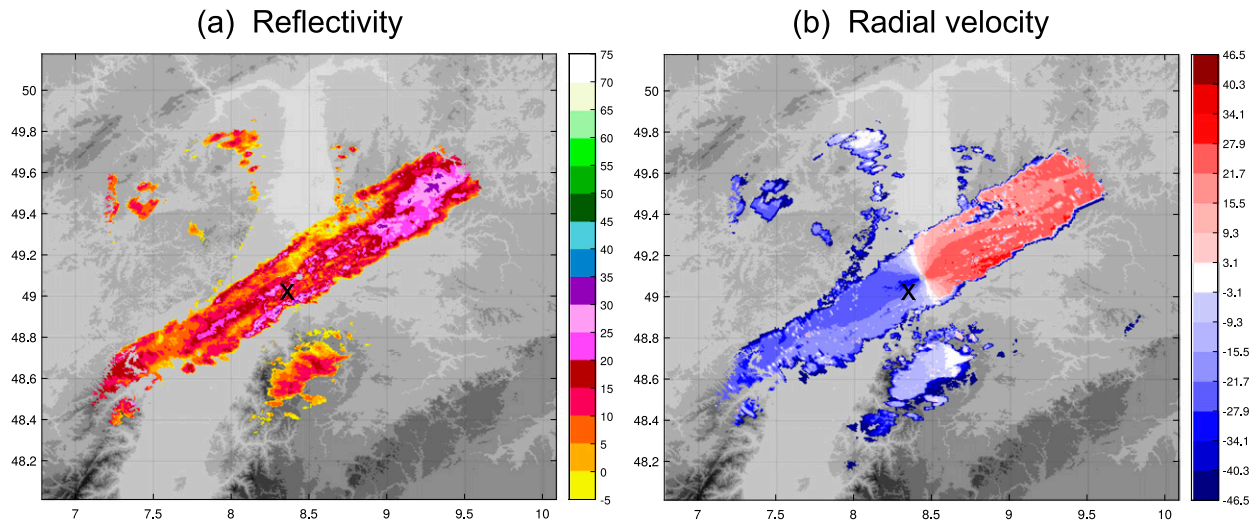


FIG. 6. (a) Reflectivity (in dBZ) and (b) radial velocity (in m s^{-1}) at 1000 m AGL derived from the KIT Doppler radar at 1645 UTC 23 Feb 2017. The radar is collocated with the instrumented tower and the observation domain approximately matches the simulation domain of the ICON outermost nest in Fig. 1. The cross marks the position of the Doppler lidar.

It precedes a rapid decrease down to 11°C at 1700 UTC (C), which is clearly enhanced through evaporative cooling by the precipitation line observed by the KIT radar (Fig. 6a). The dewpoint (Fig. 4d) also shows a peculiar evolution, as it drops by 6°C within 30 min during the peak of temperature at 1330 UTC (A), resulting in relative humidity below 30%, before it quickly rises again by 4°C during the passage of the precipitation line until 1700 UTC (C). This evolution is observed simultaneously at all levels of the KIT tower, as well as at the DWD station despite an earlier timing and a wet shift of about 2°C probably due to the proximity of a small lake. The dry period 1330–1700 UTC contains the passage of the cold front of Thomas, as indicated by the minimum of 985 hPa reached by surface pressure at 1530 UTC (B in Fig. 4e). The beginning and ending of the dry period are also marked by kinks in the pressure evolution at 1330 and 1700 UTC (A and C).

These observations allow explaining the dynamics of recorded wind peaks (Figs. 4a,b; see also labels A–D in Figs. 2 and 3). The sharp 1700 UTC peak (C) is clearly due to the downward mixing of high momentum during the passage of the precipitation line, which reaches both tower and surface station. The sharp 1800 UTC peak (D) and following wind maxima are also due to downward mixing related to precipitation but in the form of isolated showers (not shown), which explains the observed variability in timing and amplitude as expected for convective gusts. Earlier, the broad 1530 UTC peak (B) corresponds to the timing of the cold frontal passage and indicates the presence of the warm conveyor belt jet of Thomas. In contrast to these known sources of strong

winds in extratropical cyclones (Parton et al. 2010), the reason for the first peak at 1330 UTC (A) is less straightforward and is further investigated in section 3c.

Finally, besides time series from single instruments, combining wind and temperature measurements from different heights at the KIT tower provides the bulk Richardson number Ri [Eq. (1); Fig. 4f]. The resulting values reveal that the boundary layer remains turbulent during the whole day—driven either by shear ($0 < Ri < 0.25$) or by buoyancy ($Ri < 0$)—and close to neutral stability ($Ri \approx 0$) during all four wind peaks (A–D). Note that the exact value of Ri depends on the heights used for its computation, which can result in marginal stability or instability, but the evolution remains consistent altogether (blue and green curves for the layers 30–100 and 30–200 m AGL, respectively). The bulk Richardson number shows a clear change from near-neutral stability at night ($Ri \approx 0$) to thermal instability in the morning following sunrise around 0630 UTC. Near-neutral stability is again found from the beginning of the dry period at 1330 UTC onward (A). A partial return to thermal stability already occurs near 1130 UTC and matches a first and weaker drop in dewpoint with an amplitude of about 1°C (Fig. 4d) as well as the downward mixing of strong winds measured by lidar (Fig. 5a).

b. Model evaluation

Time series of variables observed at the DWD surface station in Rheinstetten are extracted from model forecasts and simulations, both to assess the local predictability of storm Thomas and to better understand the

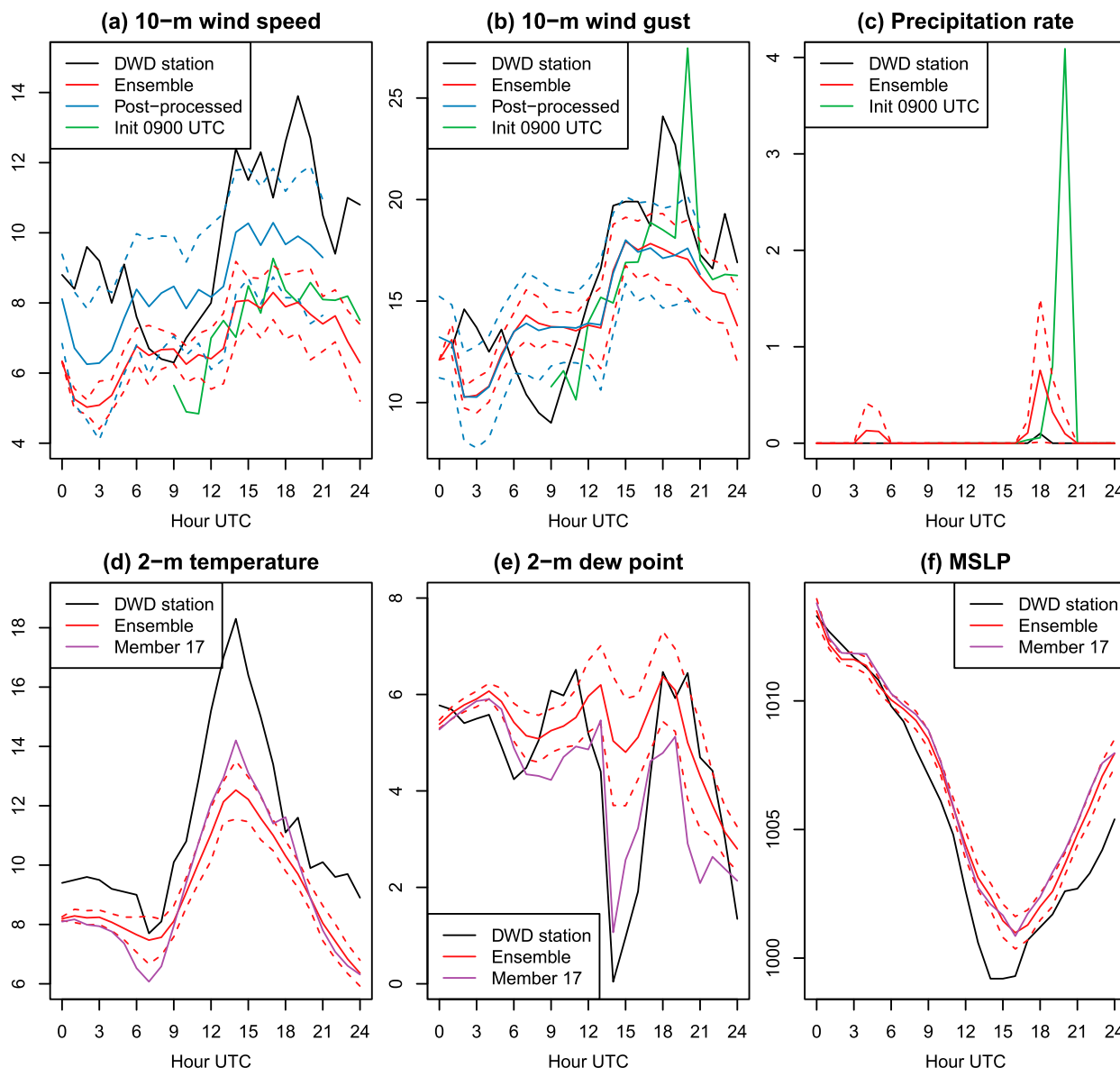


FIG. 7. Time series of operational COSMO-DE forecasts at the DWD station on 23 Feb 2017: (a),(b) 10-m wind speed and gusts (in m s^{-1}); (c) precipitation rate (in mm h^{-1}); (d),(e) 2-m temperature and dewpoint (in $^{\circ}\text{C}$); and (f) mean sea level pressure (in hPa) for the raw ensemble (red lines), postprocessed ensemble [blue lines in (a),(b)], deterministic forecast initialized at 0900 UTC [green lines in (a)–(c)], and ensemble member 17 [violet lines in (d)–(f)] compared with hourly observations (black lines). The ensemble forecast, which is initialized at 0000 UTC 23 Feb 2017, is depicted by its mean and standard deviation (solid and dashed lines).

dynamics at the WASTEX site. Selected ensemble and deterministic forecasts are shown in Fig. 7 for the operational 2.8-km COSMO-DE prediction system, while ICON large-eddy simulations at different resolutions are shown in Fig. 8.

First, COSMO-DE forecasts underestimate the observed 10-m wind speed during most of the day with an average bias of -2.8 m s^{-1} in the ensemble mean (solid red curve in Fig. 7a). The underestimation is not specific

to the case study of storm Thomas but systematically stands out in COSMO-DE ensemble forecasts at that location (Pantillon et al. 2018a). In contrast, forecasts better capture the intensity of 10-m wind gusts with a smaller average bias of -1.2 m s^{-1} in the ensemble mean (solid red curve in Fig. 7b). Such a discrepancy between the bias of wind speed and gusts has already been shown in COSMO-DE ensemble forecasts (Pantillon et al. 2018a), which suggests compensating errors in the

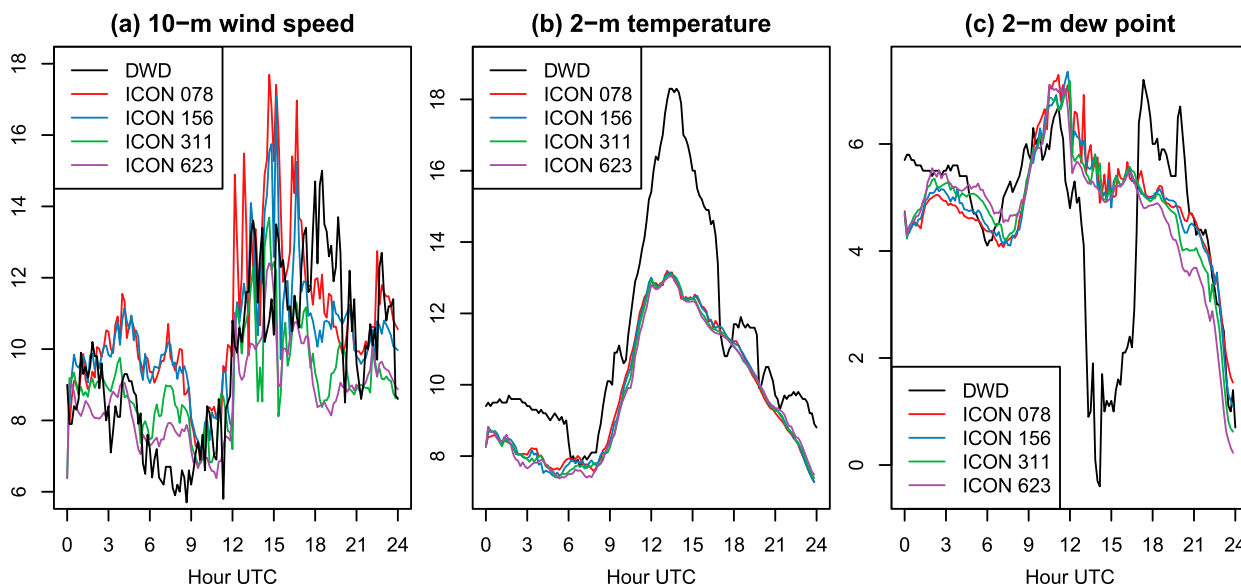


FIG. 8. Time series of ICON large-eddy simulations at the DWD station on 23 Feb 2017: (a) 10-m wind speed (in m s^{-1}) and (b),(c) 2-m temperature and dewpoint (in $^{\circ}\text{C}$) in the 78-m (red curves), 156-m (blue curves), 311-m (green curves), and 623-m simulations (violet curves) compared with 10-min observations (black curves).

gust parameterization here. Applying statistical postprocessing to the ensemble forecasts using several years of training data allows correction of any systematic error (see section 2b). Accordingly, the underestimation in wind speed is reduced to -1.1 m s^{-1} and the results are more consistent with wind gusts, for which the ensemble mean is barely affected (solid blue curves in Figs. 7a,b). Applying statistical postprocessing also increases the ensemble spread, which better encompasses observations (dashed curves in Figs. 7a,b).

However, large errors persist in the evolution of wind speed and gusts. Even with statistical postprocessing, both variables remain underestimated at night until 0600 UTC and in the afternoon and evening from 1200 UTC onward, while they become overestimated in between (i.e., during the calm morning). Furthermore, the two observed peaks in gusts at 1800 and 1900 UTC are missed by forecasts. As discussed above, these peaks are related to postfrontal precipitation taking the form of a line (Fig. 6a) and isolated showers. Only the deterministic forecast initialized at 0900 UTC captures a strong gust associated with intense precipitation at 2000 UTC (green curve in Figs. 7b,c). This illustrates the challenge of accurately forecasting convective gusts at the right place and time, even at convection-permitting resolution.

The 2-m temperature predicted by COSMO-DE also presents an overall underestimation compared to observations during the course of the day with an average bias of -2.2°C in the ensemble mean (solid red curve in

Fig. 7d). The underestimation may partly be systematic but its amplitude increases beyond 5°C at 1400 UTC. Statistical postprocessing is not applied here, because the method has been developed for wind speed and gust only (Pantillon et al. 2018a). In contrast to temperature, the predicted 2-m dewpoint shows a weak overestimation of 0.7°C in the ensemble mean (solid red curve in Fig. 7e). However, most forecasts largely miss the sudden drop observed between 1300 and 1400 UTC and only few ensemble members nearly capture its amplitude (e.g., member 17; violet curve).

Furthermore, the predicted pressure is too high from 0600 UTC onward compared to observations, an average bias of 1.2 hPa in the ensemble mean indicating a slightly too weak cyclone (solid red curve in Fig. 7f). Finally, the rain is overestimated overall, both during the passage of the precipitation line and showers in the afternoon, and during a weaker peak that is not observed in the morning (Fig. 7c). These results generally indicate a moderate predictability of local conditions in operational forecasts during the passage of storm Thomas at the WASTEX site.

The quality of ICON simulations is also assessed against standard meteorological observations at the DWD surface station. However, while operational COSMO-DE forecasts are limited by their hourly output frequency, ICON simulations are compared with the original 10-min frequency of observations to better investigate the representation of local processes. Note that wind gusts were not output and are thus not

assessed here. Time series of 10-m wind speed show that ICON simulations capture well the magnitude of observations (Fig. 8a). They also predict the observed time evolution with a first decrease in wind speed in the morning followed by a sharp increase at noon and a new decrease in the evening. Comparing the four ICON simulations among each other further shows that the model resolution directly impacts the intensity (Fig. 8a) and the average bias ranges from -1.0 m s^{-1} in the 623-m simulation to 1.1 m s^{-1} in the 78-m simulation.

Despite these biases, ICON simulations generally perform better than COSMO-DE forecasts, which largely underestimate the wind speed and miss its decrease in the morning (Fig. 7a). When model outputs are coarsened to the same 2.8-km horizontal grid, the wind speed is reduced by 0.7 m s^{-1} on average in ICON simulations but the total bias remains smaller than for COSMO-DE forecasts (not shown). This highlights the added value of large-eddy simulations compared to convection-permitting forecasts to predict local winds during a storm. In contrast to these promising results for wind speed, however, other meteorological variables suffer the same biases in ICON simulations as in COSMO-DE forecasts. The 2-m temperature is also underestimated by more than 5°C during the afternoon and does not show a clear sensitivity to the model resolution (Fig. 8b). The sudden drop in 2-m dewpoint at 1330 UTC is also missed by all ICON simulations and increasing the resolution does not lead to any clear improvement (Fig. 8c). Furthermore, the observed precipitation line at 1645 UTC (Fig. 6a) and subsequent postfrontal showers are absent from ICON simulations (not shown), which miss the associated peaks in wind, drops in temperature, and increases in dewpoint (Fig. 8). These results emphasize that large-eddy simulations inherit limitations from the parent model for the representation of mesoscale processes and, for some aspects, can even perform worse.

c. Downward mixing of dry air

The reasons for the sudden drop in dewpoint between 1300 and 1400 UTC are investigated based on COSMO-DE ensemble member 17, which—at least partially—predicts its amplitude (violet curve in Fig. 7e). This member is also more successful than most other forecasts at predicting the amplitude of the warming between 0700 and 1400 UTC (violet curve in Fig. 7d). Note, however, that it overestimates wind speed and gusts in the morning (not shown), is too cold and dry overall (Figs. 7d,e) and is not better than other ensemble members at capturing the pressure deepening (Fig. 7f). The focus

here is thus on the evolution of dewpoint in the early afternoon.

A map of 2-m dewpoint predicted by ensemble member 17 at 1200 UTC reveals that dry air is present near the surface downstream of mountain ranges (Fig. 9a). This is most striking along the northerly flank of the Swabian Jura (around $48^\circ 20' \text{N}$, 9°E) but also affects the Upper Rhine Valley to the east of the Vosges Mountains (around 48°N , $7^\circ 30' \text{E}$; see also Fig. 1 for the location and orography of mountain ranges). At that time, the WASTEX site (near 49°N , $8^\circ 30' \text{E}$) lies at the northern end of a strip of moist air that moves eastward but still separates the two areas of dry air. The predicted pattern agrees well with observations from the DWD surface stations in the region (colored dots), although the model tends to be too moist at that time. Consistent with this pattern in dewpoint, the predicted 2-m temperature shows warm air downstream of the Vosges Mountains, Black Forest, and Swabian Jura (Fig. 9b). It also agrees with station observations (colored dots) despite an overall cold bias.

The surface dry air originates from the warm and dry layer in the lower troposphere already emphasized in the COSMO-DE analysis at 1200 UTC (Figs. 3c,d). A time evolution of hourly vertical profiles in ensemble member 17 at the WASTEX site suggests that the dry layer forms in the morning and is mixed downward to the surface at 1400 UTC (Fig. 9d), which explains the sudden drop in dewpoint at that time (Fig. 7e). Vertical profiles of model temperature further highlight the presence of a temperature inversion associated with the dry layer in the morning (dashed line in Fig. 9e). The inversion appears to prevent the downward mixing of dry air until it weakens in the early afternoon.

Local conditions simulated at the WASTEX site can be compared to observations from two radiosoundings at 1200 UTC released by DWD in the surroundings (black and blue curves in Fig. 10; see diamonds in Fig. 1 for their location). Both radiosoundings emphasize the dry layer up to 550 hPa accompanied by a low-level jet maximum above 30 m s^{-1} around 700 hPa. However, while the dry layer reaches the surface in Stuttgart (located about 65 km east-southeastward of the WASTEX site; Fig. 10b), it is isolated from a moist layer below 850 hPa by a strong temperature inversion in Idar-Oberstein (located about 100 km northwestward; Fig. 10a). This contrast is well captured by ensemble member 17, although the simulated inversion level is too low and vertical gradients too smooth (red and magenta curves in Fig. 10b). The situation at the WASTEX site at 1200 UTC is thus similar to that in Idar-Oberstein but then evolves toward the situation in Stuttgart.

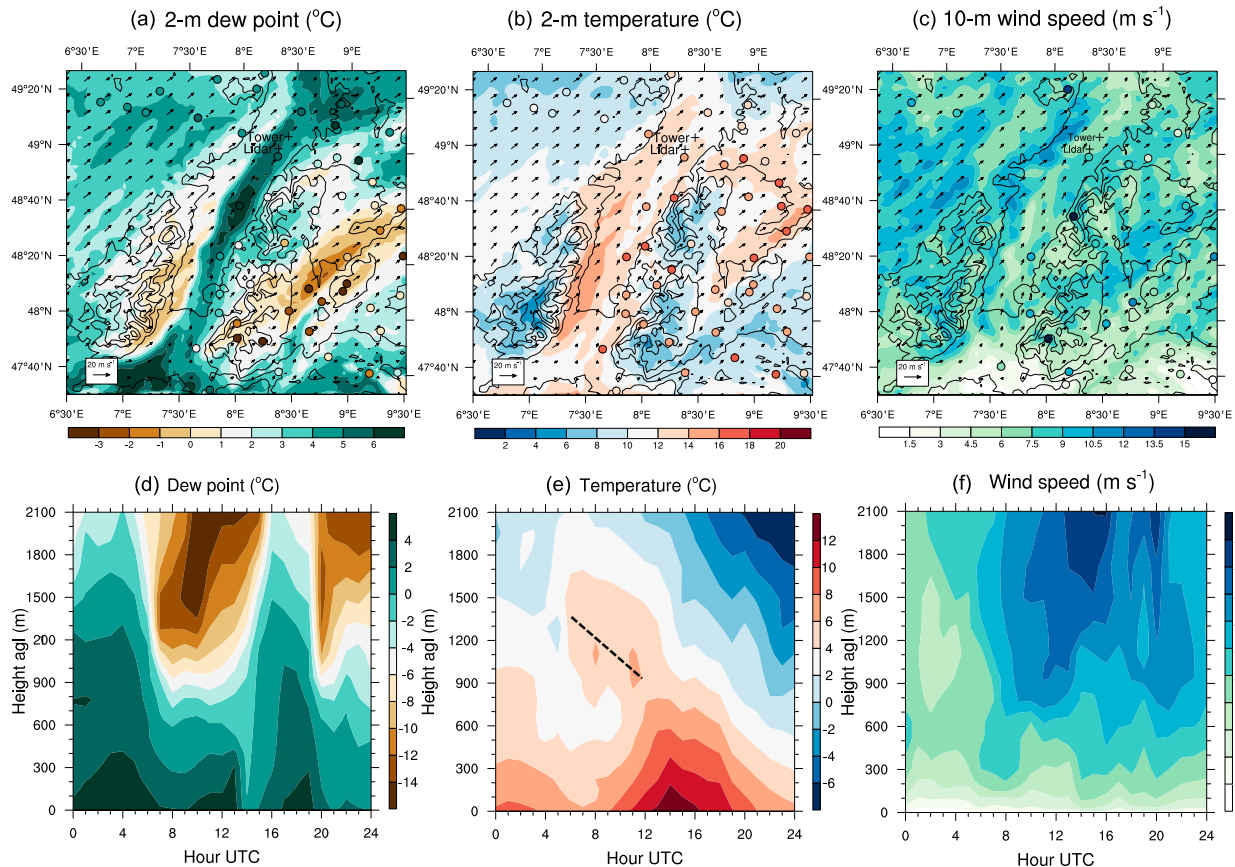


FIG. 9. Regional dynamics in COSMO-DE ensemble member 17 on 23 Feb 2017: (a),(d) dewpoint (in $^{\circ}\text{C}$); (b),(e) temperature (in $^{\circ}\text{C}$); and (c),(f) wind speed (in m s^{-1}) shown in near-surface maps at (a)–(c) 1200 UTC over the Upper Rhine Valley and (d)–(f) in hourly vertical profiles at the WASTEX site. Colored dots in (a)–(c) indicate observations from all available DWD surface stations in the area and contours show the model orography each 200 m. Refer back to Fig. 1 for details of the orography.

The dry layer that forms in the morning above 700 m AGL and from 0600 UTC onward is associated with strong winds in ensemble member 17 (Figs. 9d,f), in agreement with the formation of a low-level jet observed by Doppler lidar (Fig. 5a). The strong winds in the morning are also isolated by the temperature inversion and the downward mixing of dry air at 1400 UTC implies the transfer of high momentum to the surface (Figs. 9d,f). This is consistent with the presence of a small region of higher surface winds to the west of the WASTEX site that moves eastward with the region of dry air (Figs. 9a,c). The transfer of high momentum to the surface thus contributes to the observed and predicted peak in 10-m wind speed and gusts at 1400 UTC (Figs. 7a,b).

Altogether, the evolution of local conditions is reminiscent of the breakthrough of foehn in Alpine valleys, which is known to be a challenge for numerical weather prediction systems (Richner and Hächler 2013). However, foehn events are unlikely at the WASTEX site, considering the mostly flat terrain in

the direct surroundings and the far distance to the Vosges Mountains (Fig. 1). Furthermore, the near-surface temperature increases progressively during the hours preceding the sudden drop in dewpoint (Figs. 4c,d), which does not match the expected warming during a typical foehn event. Nevertheless, the pattern of near-surface dry air downstream of mountain ranges in ensemble member 17 clearly indicates an orographic contribution upstream of the WASTEX site (Fig. 9a) and a wave pattern over the warm sector can be recognized in satellite imagery (Fig. 2).

Accordingly, mountain waves with wavelength of about 20 km are found in the lee of the Vosges Mountains in ensemble member 17 (Fig. 11a). Their amplitude decreases at the northern tip of the mountain range, where the orography is lower. The waves extend vertically over the whole troposphere and tilt upwind with height in the lower stratosphere, which clearly indicates that they propagate upward, while they also affect vertical velocities and potential temperature over several wavelengths downstream (Fig. 11b).

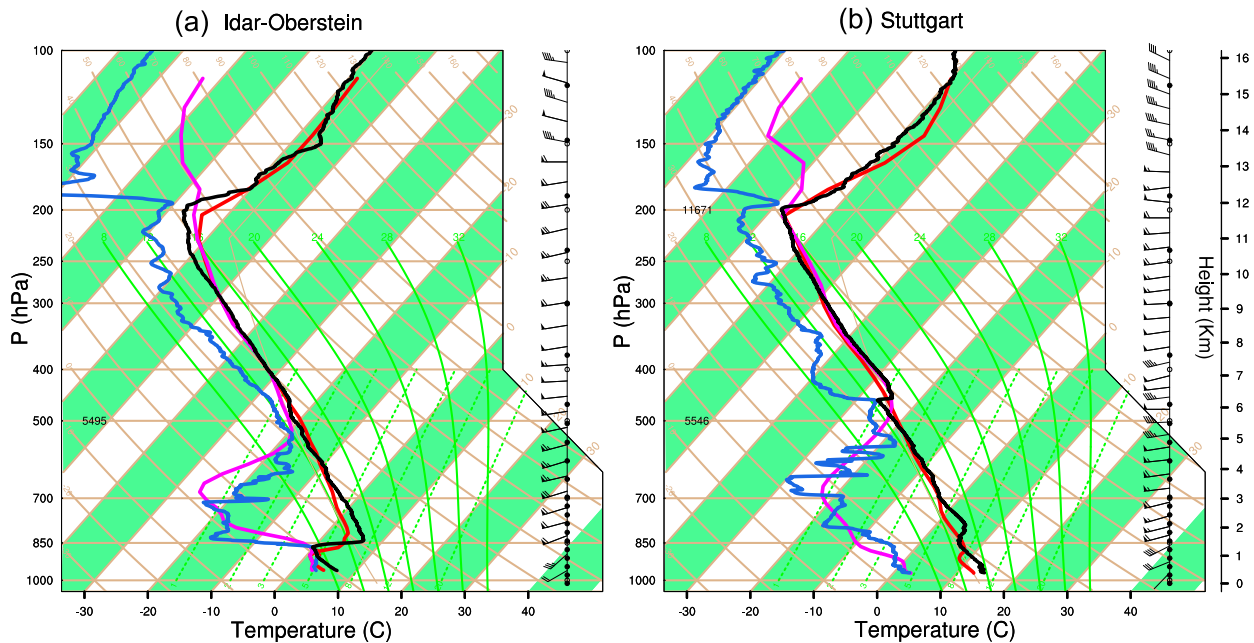


FIG. 10. Skew T -log p diagrams at (a) Idar-Oberstein and (b) Stuttgart at 1200 UTC 23 Feb 2017 from DWD radiosoundings (black and blue curves) and from COSMO-DE ensemble member 17 (red and pink curves). Their locations are marked by diamonds in Fig. 1.

It is unclear whether the amplitude of mountain waves is sufficient to contribute to the downward mixing at the WASTEX site (vertical line) or if wave breaking rather occurs closer to the Vosges Mountains and is advected downstream. The effect of mountain waves

likely combines with boundary layer convection and turbulent erosion from strong shear aloft to remove the temperature inversion. This combination is similar to a case study of strong westerly flow over the mountainous island of Corsica discussed in Adler and

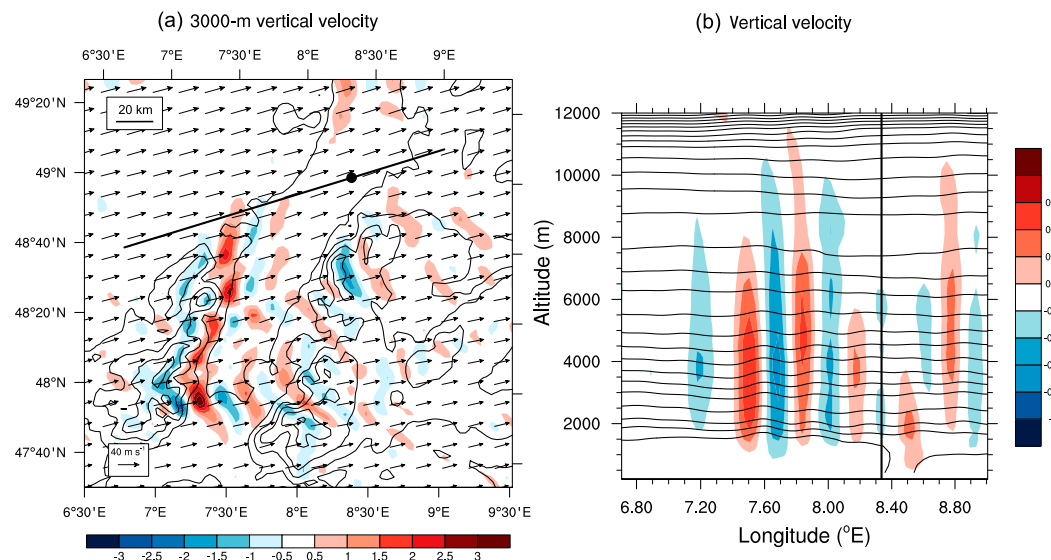


FIG. 11. Mountain waves in COSMO-DE ensemble member 17 at 1400 UTC 23 Feb 2017: vertical velocity at (a) 3000-m altitude over the Upper Rhine Valley and (b) in a vertical cross section aligned with the wind at the WASTEX site. Contours show the model orography every 200 m in (a) and the potential temperature every 2 K in (b). The line in (a) marks the trace of the cross section and the point in (a) and vertical line in (b) indicate the location of the WASTEX site. Refer back to Fig. 1 for details of the orography.

Kalthoff (2016). Note that other such events were not observed during the WASTEX field campaign.

5. Structure of the boundary layer winds

a. Doppler lidar observations

The high spatial and temporal resolution of Doppler lidar observations is exploited in distance–time (Hovmöller) and time–height sections to investigate the finescale structure of boundary layer winds (Fig. 12; see animation S1 in the online supplemental material for individual scans). The focus here is on the time period 1100–1400 UTC (i.e., the storm onset). As highlighted by averaged measurements in Fig. 5a, the wind starts strengthening near 1130 UTC due to downward transfer of momentum from the low-level jet. However, high-resolution measurements reveal that the strengthening is not regular but occurs as two bursts of strong wind that reach the lidar near 1145 and 1155 UTC and are seen as two slanted stripes in a distance–time plot at 100 m AGL (circles in Fig. 12a; see also animation S1). The bursts last for 7–8 min while traveling over the whole horizontal range of nearly 5 km. Their slope gives an approximate translation speed of 10 m s^{-1} , which roughly corresponds to the mean radial wind at that height and thus suggests that they are advected by the background flow. The two bursts are also clearly seen in a time–height plot at a distance of 2.5 km, where they extend vertically over the whole range of more than 600 m (circles in Fig. 12b).

Regular stripes are further observed in a distance–time plot during the next hour from 1200 to 1300 UTC (Fig. 12c). They reveal the presence of long-lasting structures of strong wind advected by the background flow, similar to the initial bursts. The presence of structures is also apparent in a time–height plot, across the whole observed height until 1230 UTC but less obvious above 100–200 m AGL afterward (Fig. 12d). Between 1300 and 1330 UTC, three successive bursts of strong wind are observed extending over several 100 m in height (circles in Figs. 12e,f). These bursts mark the end of the period characterized by long-lasting structures. From 1330 UTC onward they give place to a patchy pattern of smaller structures that last for less than a minute and travel a few 100 m only (Fig. 12e; see also animation S1). The new pattern dominates for the next hours, before striped patterns shortly reappear during an increase in wind speed related to the passage of the cold front around 1530 UTC and later during the wind maximum associated with precipitation around 1700 UTC (not shown).

Although surface wind measurements are not available along the lidar path, the observed structures of strong winds are expected to result in strong gusts. This suggests

potential for gust nowcasting, as the structures can clearly be followed several minutes in advance (Figs. 12a,c,e). Note that individual structures would likely not be recognized in time series of wind and gusts from surface stations, because their separation in time is shorter than the standard 10-min sampling. Interestingly, the time of transition from coherent to transient structures in distance–time plots around 1330 UTC (long- and short-lasting structures, respectively) corresponds to the first peak in winds and gusts, the sudden drop in dewpoint, and the return to near-neutral stability, while the earlier appearance of coherent structures near 1130 UTC matches the weaker drop in dewpoint associated with an increase in bulk Richardson number (Fig. 4).

Previous studies have proposed different objective methods to identify coherent wind structures in observational datasets. For instance, Barthlott et al. (2007) used wavelets transforms for time series from an instrumented tower, while Brilouet et al. (2017) applied a spectral analysis to airborne measurements, and Zhou et al. (2018) clustered values above a certain threshold in two-dimensional Doppler lidar observations. Here we try an alternative method to identify coherent wind structures based on the extraction of ridge surfaces in the distance–height–time space of measurements. In this three-dimensional space, a two-dimensional ridge is defined as the set of points where the first derivative is zero and the second derivative is negative (i.e., local maxima) in the direction given by the first eigenvector of the Hessian matrix (Lindeberg 1998; Eberly 2012). The results are illustrated in animation S2 for the period 1200–1500 UTC. During the first half of the period until 1330 UTC, parallel ridge surfaces in the three-dimensional space confirm the presence of structures that remain coherent in space and time. In contrast, surfaces during the second half of the period after 1330 UTC show smaller extent, higher curvature, and more variable orientation, which indicate a loss of coherence.

The evolution from 1200 to 1500 UTC is summarized in Fig. 13a as the orientation of all local ridge surfaces in a distance–time plane, expressed as radial velocity (equivalent to the slope of stripes in Figs. 12a,c,e). The distribution exhibits large spread due to local heterogeneities but clearly peaks between 10 and 15 m s^{-1} from 1200 to 1300 UTC (blue bars), which matches the mean wind speed and confirms that structures are mainly advected by the background flow at that time. In contrast, the distribution is broader and peaks between 0 and 5 m s^{-1} from 1400 to 1500 UTC (green bars), which indicates that structures lack coherence in time and space. An intermediate situation is found from 1300 to 1400 UTC (orange bars), which is consistent

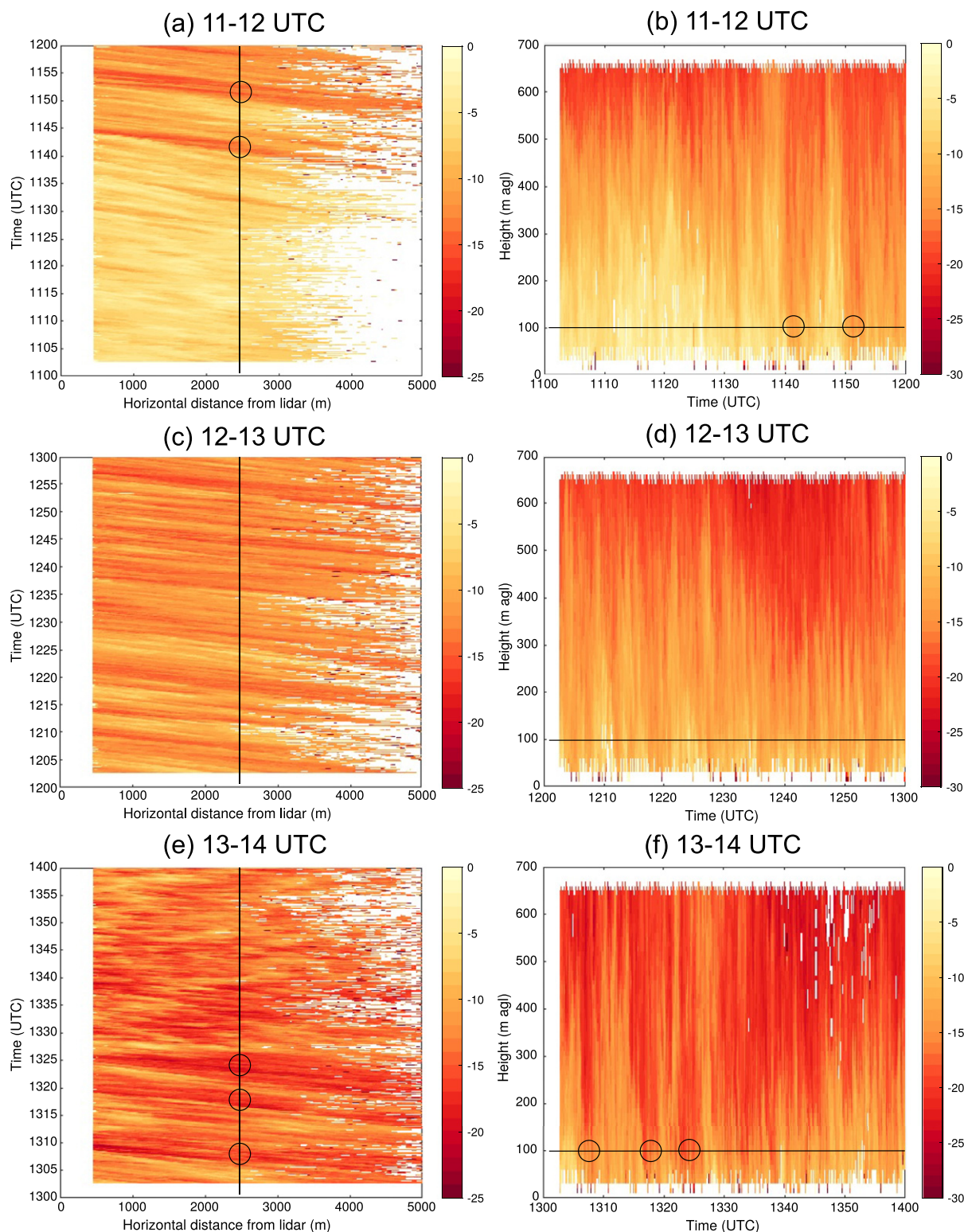


FIG. 12. High-resolution radial wind (in m s^{-1}) as measured by Doppler lidar in (a),(c),(e) hourly distance–time (Hovmöller) plots at a height of 100 m AGL and (b),(d),(f) time–height plots at a distance of 2500 m from (a),(b) 1100–1200 UTC; (c),(d) 1200–1300 UTC; and (e),(f) 1300–1400 UTC 23 Feb 2017. Vertical and horizontal lines mark the 2500-m distance and 100-m AGL height, respectively, while circles indicate bursts of strong wind.

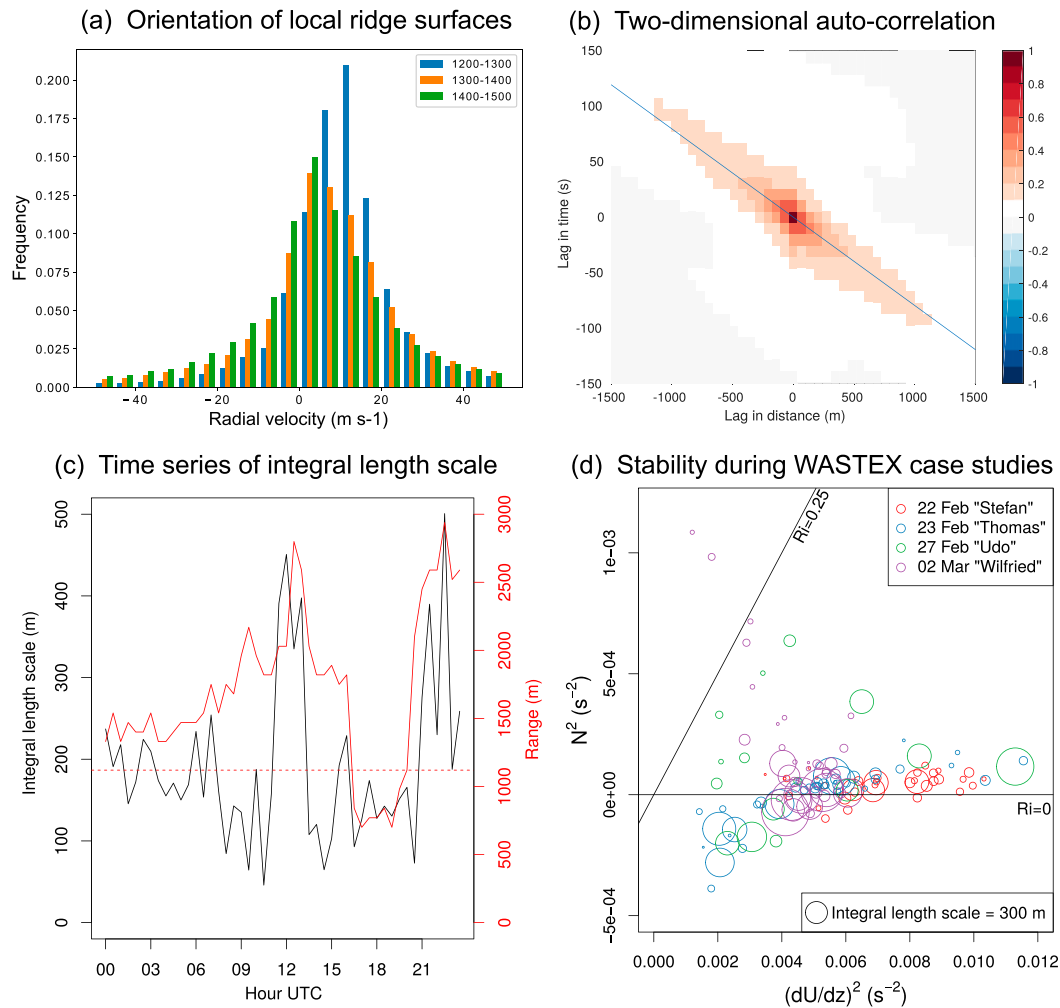


FIG. 13. Coherent structures in Doppler lidar measurements: (a) hourly distributions of the orientation of local ridge surfaces from 1200 to 1500 UTC, (b) two-dimensional autocorrelation in a distance–time section at 100 m AGL from 1230 to 1300 UTC, (c) time series of integral length scale and measurement range over 30-min periods on 23 Feb 2017, and (d) comparison with atmospheric stability for four WASTEX case studies. Local ridge surfaces used in (a) are visualized in three dimensions in animation S2. The blue line in (b) illustrates the slope of wind speed along which the integral length scale is computed. The dotted red line in (c) indicates the empirical threshold of 1100 m in range. Horizontal and slanted lines in (d) correspond to values of $Ri = 0$ and $Ri = 0.25$, respectively. See section 5a for details.

with the transition from coherent to transient structures near 1330 UTC. These three-dimensional results thus corroborate the subjective identification of coherent structures from two-dimensional plots in Fig. 12.

To complement this method based on local ridge surfaces, a more statistical approach based on integral length scales is used with the aim of linking the presence of coherent structures with atmospheric stability (see Stawiarski et al. 2015 for a comparison with wavelet and clustering methods applied to Doppler lidar data). With a similar approach, Träumner et al. (2015) found that coherent structures occur more often under stable than unstable conditions but with smaller length scales

thus confirmed earlier results by Barthlott et al. (2007). Here, integral length scales are computed in distance–time sections at 100 m AGL (as illustrated in Figs. 12a,c,e). For this purpose, the two-dimensional autocorrelation function is first computed in these sections using 30-min periods and the whole measurement range. This is exemplified in Fig. 13b for the period containing coherent structures from 1230 to 1300 UTC, when an elongated shape of positive autocorrelation aligns in distance and time with the slope of average wind speed during that period (blue line). The autocorrelation is then integrated along the slope with respect to distance to give the integral length scale.

The result is shown in Fig. 13c as a time series for the course of 23 February 2017 during the passage of Thomas. High values of integral length scale (black curve) highlight the period from 1130 to 1330 UTC to be characterized by coherent wind structures. Sharp variations at the beginning and ending of this period are consistent with the quick appearance and disappearance of structures (Figs. 12a,e). The integral length scale is also relatively high during the night compared to the morning, and increases again in the evening after 2100 UTC (Fig. 13c), in accordance with the presence of coherent structures (see animation S1). Note that Doppler lidar observations tend to smooth wind structures spatially and thus overestimate length scales (Stawiarski et al. 2015). However, the coherent structures observed here may persist beyond the measurement range, which suggests that integral length scales might actually be underestimated. In particular, the range drops at 1630 UTC due to the arrival of precipitation and does not recover before 2100 UTC (red curve in Fig. 13c). This reduces the integral length scale despite the possible presence of coherent structures. Therefore, an empirical threshold in range is set to 1100 m in order to filter out such ambiguous data (red dashed line in Fig. 13c).

Based on this statistical approach, a relationship is explored between the presence of coherent structures and atmospheric stability (Fig. 13d). The bulk Richardson number [Eq. (1)] is decomposed into squared Brunt–Väisälä frequency N^2 and vertical wind shear $(\Delta U/\Delta z)^2$ in the layer 30–100 m AGL to separate between buoyancy- and shear-driven turbulence. The analysis is extended to three extratropical cyclones that occurred during the same period as Thomas and provided good lidar observations during WASTEX: Stefan on 22 February, Udo on 27 February, and Wilfried on 2 March 2017. This allows both extending the statistics and putting Thomas in a wider context. Coherent structures are present during all four windstorms (large circles in Fig. 13d). They tend to occur in conditions of near-neutral stability and high shear ($Ri \approx 0$), which are most common during the four cases. This confirms previous results of dual-Doppler lidar measurements in strong flow (Newsom et al. 2008). However, structures also form with thermal instability and moderate shear ($Ri \ll 0$) during the onset of Thomas and during the passage of Udo (blue and green circles) and suggest the presence of boundary layer rolls (Etling and Brown 1993; Atkinson and Zhang 1996; Young et al. 2002).

b. Large-eddy simulations

High-resolution ICON simulations complement Doppler lidar observations to characterize boundary layer

winds during the onset of Thomas. Maps of near-surface winds at noon reveal the arrival of structures over the WASTEX site (Fig. 14). The structures are elongated in the wind direction and remain coherent in space and time while they are advected by the background flow (see animation S3 for the evolution from 1100 to 1400 UTC in the ICON 78-m simulation). Their intensity increases with resolution, which explains the higher variability of wind speed in time series of 78- and 156-m compared to 311- and 623-m simulations (Fig. 8a). In contrast to the intensity, the size of structures decreases with resolution and appears to scale with grid spacing (Fig. 14). While their presence becomes barely distinguishable in the 623-m simulation due to the combined effect of weakening and broadening, the width of structures reaches ≈ 1.5 km in the 78-m simulation (≈ 20 grid points). Note that neither the intensity nor the size of structures converges within the four ICON simulations. The arrival of wind structures is further linked to the arrival of drier air, which explains the associated plateau in temperature and drop in dewpoint simulated at 1200 UTC at the DWD station (Fig. 8c). These variables also exhibit coherent structures, albeit with small amplitude (not shown).

The elongated structures simulated by ICON are reminiscent of the along-wind rolls observed by Doppler radar during the passage of windstorm Christian over the United Kingdom on 28 October 2013 (Browning et al. 2015). While rolls separated by 1–3 km were found in the area of strongest winds and associated with convective showers, rolls separated by less than 1 km were found in an area of more moderate winds and associated with boundary layer convection. Although the simulated structures are broader here, they are attributed to boundary layer rolls due to the absence of precipitation and the discrepancy in size is explained by the lack of convergence with model resolution.

Now the question arises whether the simulated structures explain the coherent structures in space and time measured by Doppler lidar (Fig. 12). This question is discussed with the help of virtual observations obtained by extracting the radial wind speed from ICON simulations as a Doppler lidar would measure if it was placed at the WASTEX site and oriented to face the mean flow. Virtual observations for the 78-m simulation reproduce regular stripes from 1200 to 1400 UTC in a distance–time section at 100 m AGL (Fig. 15a). Their slope matches the mean radial wind at that height (black lines), in accordance with the advection of structures by the background flow. The slope of stripes is sensitive to the azimuth angle taken as the orientation of the mean flow (not shown). However, the amplitude of the normal wind component (red contours) remains relatively

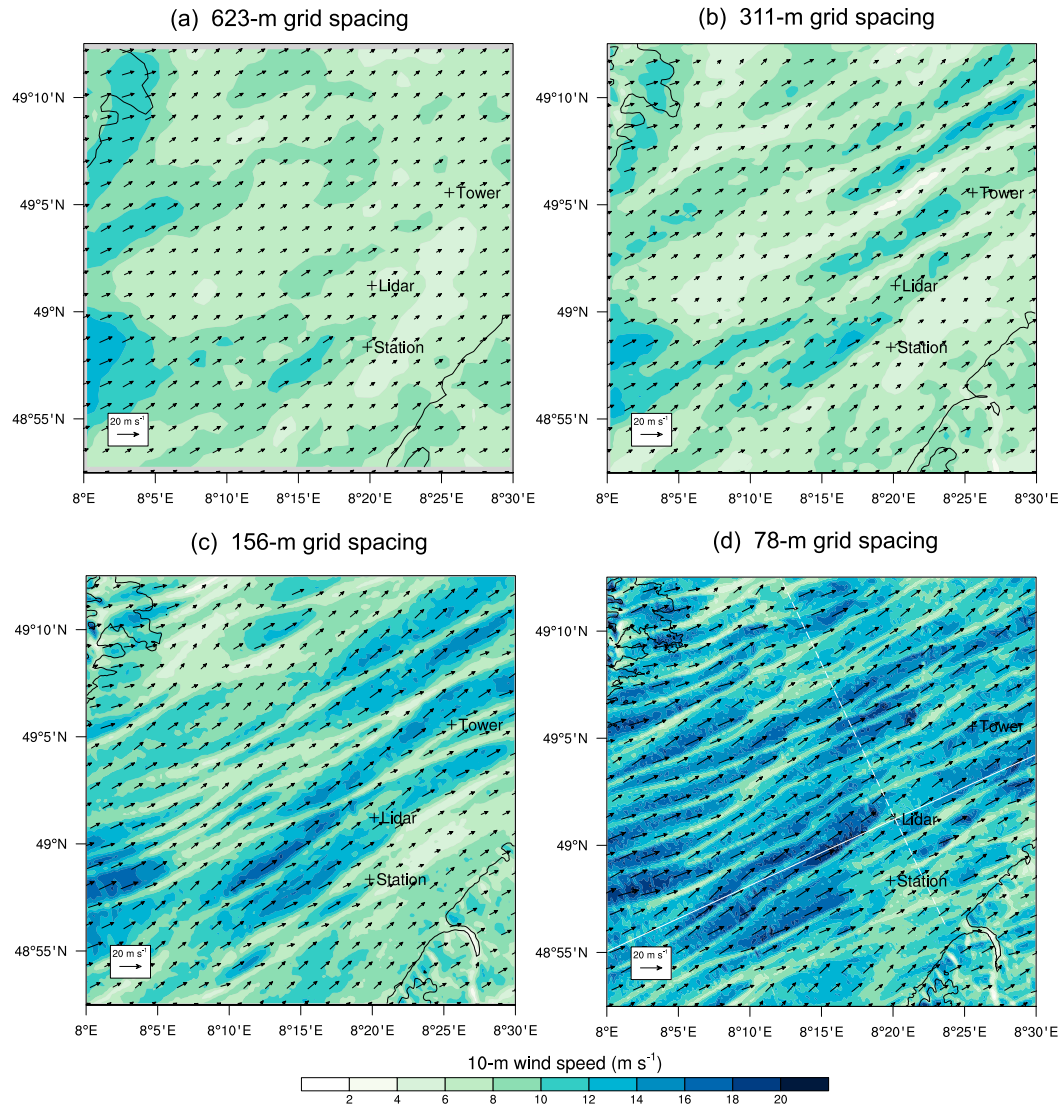


FIG. 14. Maps of 10-m wind in the surroundings of the WASTEX site in ICON (a) 623-, (b) 311-, (c) 156-, and (d) 78-m simulations at 1200 UTC 23 Feb 2017. The location of the Doppler lidar, KIT tower, and DWD station are marked and contours indicate the model topography each 200 m. Solid and dashed white lines in (d) indicate along- and cross-flow directions used for the energy spectra in Fig. 16b.

small, which suggests that the radial component is representative of the total horizontal wind. Time–height sections further show that the simulated structures are coherent over almost 1000 m in height up to a layer with stronger normal component (Fig. 15b). The increase in wind speed within the first about 100 m AGL also illustrates the vertical extent of the simulated surface layer, in which the wind is strongly affected by surface roughness.

These virtual observations qualitatively confirm that structures elongated in the wind direction can be responsible for the measured stripes in distance–time sections. The arrival of structures occurs shortly before

noon in both observations and simulations, and this is consistent with the good representation of the weak drop in dewpoint at that time (Fig. 8c). In contrast, the coherent structures persist for several hours beyond 1330 UTC in simulations instead of giving place to a patchy pattern as observed by Doppler lidar but this is also consistent with the lack of a sudden drop in the simulated dewpoint. However, the structures reproduced in virtual observations from the 78-m simulation (Fig. 15; note the 2-h displayed period) are much coarser than those actually measured (Figs. 12a,c,e) and become even coarser at lower resolution (not shown). This suggests that coherent structures are not fully captured by

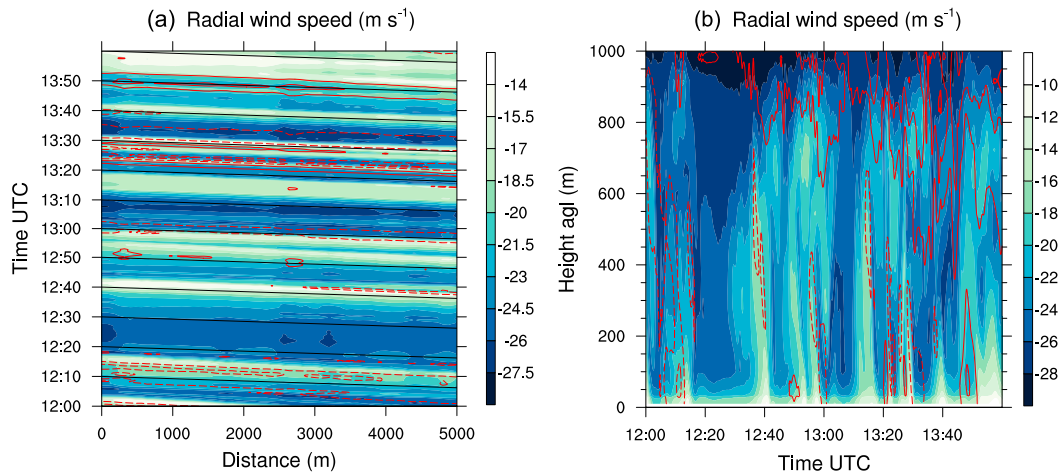


FIG. 15. Virtual Doppler lidar observations of radial wind speed in the ICON 78-m simulation from 1200 to 1400 UTC 23 Feb 2017: (a) distance–time (Hovmöller) plot on the 102-m AGL model level and (b) time–height plot at a distance of 2500 m. The distance is taken from the lidar position in the 245° direction. Black lines in (a) indicate the mean radial wind, while solid and dashed red contours show the normal wind in southeastward and north-westward directions, respectively, at 2 m s^{-1} (thin contours) and 4 m s^{-1} (thick contours).

the 78-m grid spacing, in accordance with the lack of convergence in size and intensity found in Fig. 14.

A spectral analysis is performed to provide a more quantitative assessment. First the energy spectrum with respect to frequency is investigated from time series measured and simulated at 100 m AGL at the location of the KIT tower (Fig. 16a). A minimum is apparent in spectra near 0.02 min^{-1} (period of $\approx 1 \text{ h}$), which

marks the gap between mesoscale and microscale ranges (e.g., Larsén et al. 2016). At higher frequencies, the measured spectrum peaks near 0.5 min^{-1} (period of $\approx 2 \text{ min}$), before it decreases with a slope of $-2/3$ that characterizes the inertial range (gray line). In contrast, simulated spectra peak at lower frequencies and then diverge from the observed spectrum. The divergence points logically reach higher frequencies for finer grid spacing.

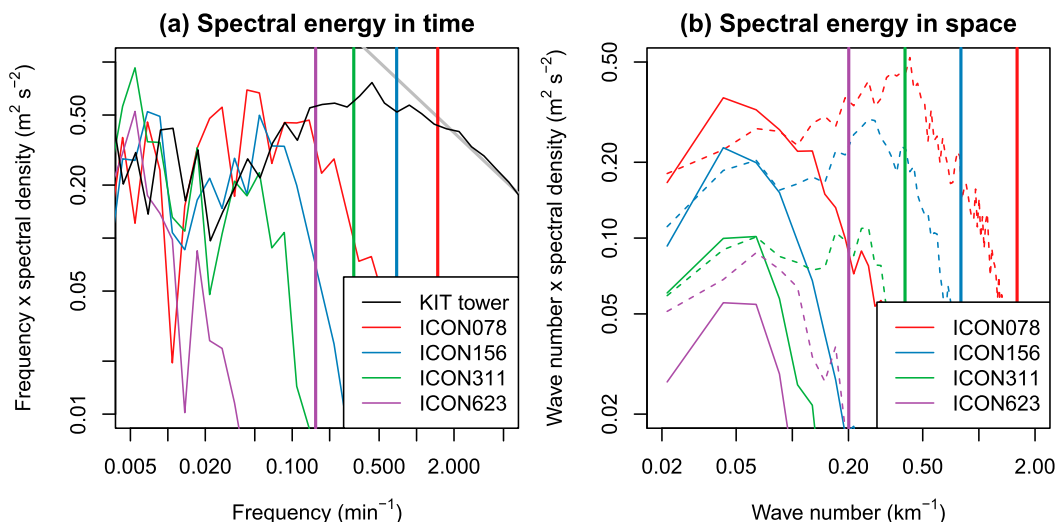


FIG. 16. Energy spectra of horizontal wind speed in ICON simulations with respect to (a) frequency and (b) wavenumber. Spectra are obtained in (a) from time series measured and simulated at 100 m AGL at the location of the KIT tower and in (b) from the 10-m wind in along-flow (solid lines) and cross-flow (dashed lines) directions as illustrated by solid and dashed white lines in Fig. 14d. Vertical lines mark the effective resolution of 8 grid points in each simulation (see text for details), while the gray line in (a) illustrates the characteristic slope of $-2/3$ of the inertial range.

A linear extrapolation suggests that—for this case study and model setup—a grid spacing of the order of $O(10)$ m would be required to reach the measured peak near 0.5 min^{-1} and likely converge in the representation of wind structures.

Energy spectra are commonly used to estimate the effective resolution of models (Baldwin and Wandishin 2002; Skamarock 2004). Using a similar setup of ICON large-eddy simulations, Heinze et al. (2017) obtained an effective resolution of approximately 8 grid points. To compare this result with the frequency of divergence points found here, the effective resolution of each simulation is computed as 8 times the grid spacing and converted to a frequency through the average wind speed at 100 m AGL at the location of the KIT tower (vertical lines in Fig. 16a). Surprisingly, the resulting values are one order of magnitude higher than the frequency of divergence points for the 78-, 156-, and 311-m simulations. The comparison is unclear for the 623-m run, because its energy spectrum drops too early. Although some uncertainty is inherent in the determination of divergence points, these values reveal a large discrepancy between the effective model resolutions and the peaks attained by simulations.

A further spectral analysis is performed with respect to wavenumber. It is computed separately in along- and cross-flow directions from the lidar position (i.e., parallel and perpendicular to the elongated structures) as illustrated by solid and dashed lines in Fig. 14d. The resulting energy spectra are displayed as solid and dashed curves in Fig. 16b. Although the divergence from a reference spectrum cannot be determined due to the absence of appropriate measurements, the drop in along-flow energy spectra at low wavenumbers (solid curves) is consistent with their frequency counterparts (Fig. 16a). In contrast, the drop in cross-flow energy spectra (dashed curves in Fig. 16b) occurs at higher wavenumbers, which is consistent with the convective circulation of boundary layer rolls and approaches closer the effective resolution of 8 grid points (vertical lines). The contrast is again weaker in the 623-m simulation, which lacks elongated structures. These results suggest that the elongation of structures is responsible for the relatively low frequency of peaks attained by simulations in energy spectra.

6. Conclusions

This paper presents a multiscale analysis of windstorm Thomas on 23 February 2017, a case study of an intense extratropical cyclone that passed the instrumented site of the WASTEX field campaign located in the Upper Rhine Valley over southwestern Germany. The formation

of gusts during the passage of the storm is sampled with a fast-scanning Doppler lidar and modeled with large-eddy simulations. These high-resolution data are complemented with classical observations from a 200-m meteorological tower, a surface station, and a C-band radar, as well as with convection-permitting deterministic and ensemble forecasts.

Four wind peaks are observed during the passage of Thomas. The first peak is related to a sudden drop in dewpoint and is due to the downward mixing of a warm and dry layer associated with a low-level jet. The downward mixing is prevented in the morning by the presence of a temperature inversion, which is later eroded by boundary layer convection from below and turbulent erosion by wind shear from above. The downward mixing moves downstream from the Vosges Mountains, which produce lee waves and appear to contribute to the downward mixing. This is poorly predicted by operational forecasts as well as large-eddy simulations and the sudden drop in dewpoint is captured by a few ensemble members only. The second peak in wind occurs during the passage of the cold front, while the third and fourth peaks are related to a precipitation line and isolated showers. The latter results in high variability in observations and low predictability in models due to the local nature of convective gusts. Overall, operational forecasts tend to underestimate the wind, while large-eddy simulations better capture its evolution and intensity but miss the arrival of precipitation.

During the storm onset leading to the first peak in wind, Doppler lidar observations reveal the presence of long-lasting wind structures advected by the background flow. These structures appear during a weak drop in dewpoint and vanish during the downward mixing of dry air. This period lasts for two hours and is marked by a combination of convective instability and moderate vertical shear. Coherent wind structures are also observed in three other cases studies of windstorms sampled during WASTEX but mostly occur in conditions of near-neutral stability and strong shear (i.e., $Ri \approx 0$). In contrast, the formation of coherent structures during the onset of Thomas is attributed to boundary layer rolls. Large-eddy simulations also exhibit coherent structures elongated in the wind direction during storm onset. Their size and intensity depend on the model resolution and are barely visible with 623-m grid spacing, while they do not converge even with 78-m grid spacing. A spectral analysis suggests that a grid spacing of the order of $O(10)$ m would be required to fully resolve the structures, the size of which largely exceed the effective model resolution. This is due to the elongation of structures, which is expected to increase with wind speed (Barthlott et al. 2007; Träumner et al. 2015)

thus modeling coherent structures during extreme windstorms may require even finer grid spacing.

The presence of coherent structures has mixed implications for predicting gusts during windstorms. On the one hand, their appearance during a storm onset shows the potential of Doppler lidar instruments to anticipate the arrival of strong gusts a few minutes in advance. This supports the use of such instruments for wind energy applications, where a sharp increase in intensity can be damaging (Bos et al. 2016). On the other hand, the presence of coherent structures is challenging for numerical weather prediction models, because they are not resolved but their size overlaps with the grid spacing. This calls for the development of appropriate parameterizations between grid-scale winds and subgrid-scale turbulence (Aksamit and Pomeroy 2018). When sufficient computing power is available, large-eddy simulations offer a solution not only to capture the formation of coherent structures but also to improve the representation of local wind intensity and evolution compared to convection-permitting forecasts. However, they inherit biases in mesoscale dynamics from the parent model, which in turn govern the presence of coherent structures. Only large-eddy simulations over large domain such as in Heinze et al. (2017) will solve these issues for extratropical cyclones by encompassing the contribution of different scales to the formation of local gusts. They will, however, require adequate measurements such as taken by Doppler lidar instruments or other innovative systems to complement the sparse existing networks of wind observations.

Acknowledgments. The authors thank Pia Bogert, Melissa Körlin, and Irina Solodovnik for processing lidar data, Jan Handwerker for providing radar observations as well as colleagues from KIT and LA for discussions that helped shaping the paper. The paper also benefitted from detailed and constructive comments from three anonymous reviewers and the editor. The City of Karlsruhe is acknowledged for hosting the Doppler lidar on the measurement site, DWD for providing COSMO-DE model data and observations from radiosoundings and from the surface network through the CDC, and NASA for satellite imagery through the Worldview application (<https://worldview.earthdata.nasa.gov>), part of the EOSDIS. Doppler lidar measurements during the WASTEX field campaign and 3D wind from the ICON 78-m simulation are available on the KITopenData repository, doi:10.5445/IR/1000096609 and doi:10.5445/IR/1000096627. Additional data are available on request to the authors. The research leading to these results has been conducted within subproject C5 “Forecast uncertainty for peak surface gusts associated with

European cold-season cyclones” of the Transregional Collaborative Research Center SFB / TRR 165 “Waves to Weather” funded by the German Research Foundation (DFG). Statistical postprocessing on Figs. 7a and 7b was provided by Sebastian Lerch from subproject C7 “Statistical postprocessing and stochastic physics for ensemble predictions,” while visualization of structures on animation S2 and Fig. 13a was provided by Peter Hügel, Florian Fallenbüchel, and Filip Sadlo from subproject A7 “Visualization of coherence and variation in meteorological dynamics.”

REFERENCES

- Adler, B., and N. Kalthoff, 2016: The impact of upstream flow on the atmospheric boundary layer in a valley on a mountainous island. *Bound.-Layer Meteor.*, **158**, 429–452, <https://doi.org/10.1007/s10546-015-0092-y>.
- Aksamit, N. O., and J. W. Pomeroy, 2018: The effect of coherent structures in the atmospheric surface layer on blowing-snow transport. *Bound.-Layer Meteor.*, **167**, 211–233, <https://doi.org/10.1007/s10546-017-0318-2>.
- Atkinson, B. W., and J. W. Zhang, 1996: Mesoscale shallow convection in the atmosphere. *Rev. Geophys.*, **34**, 403–431, <https://doi.org/10.1029/96RG02623>.
- Baldauf, M., A. Seifert, J. Förstner, D. Majewski, M. Raschendorfer, and T. Reinhardt, 2011: Operational convective-scale numerical weather prediction with the COSMO model: Description and sensitivities. *Mon. Wea. Rev.*, **139**, 3887–3905, <https://doi.org/10.1175/MWR-D-10-05013.1>.
- Baldwin, M. E., and M. S. Wandishin, 2002: Determining the resolved spatial scales of Eta model precipitation forecasts. *19th Conf. on Weather Analysis and Forecasting/15th Conf. on Numerical Weather Prediction*, San Antonio, TX, Amer. Meteor. Soc., 3.2, https://ams.confex.com/ams/SLS_WAF_NWP/techprogram/paper_47735.htm.
- Barthlott, C., P. Drobinski, C. Fesquet, T. Dubos, and C. Pietras, 2007: Long-term study of coherent structures in the atmospheric surface layer. *Bound.-Layer Meteor.*, **125**, 1–24, <https://doi.org/10.1007/s10546-007-9190-9>.
- Bos, R., A. Giyanani, and W. Bierbooms, 2016: Assessing the severity of wind gusts with lidar. *Remote Sens.*, **8** (9), <https://doi.org/10.3390/rs8090758>.
- Brasseur, O., 2001: Development and application of a physical approach to estimating wind gusts. *Mon. Wea. Rev.*, **129**, 5–25, [https://doi.org/10.1175/1520-0493\(2001\)129<0005:DAAOAP>2.0.CO;2](https://doi.org/10.1175/1520-0493(2001)129<0005:DAAOAP>2.0.CO;2).
- Brilouet, P.-E., P. Durand, and G. Canut, 2017: The marine atmospheric boundary layer under strong wind conditions: Organized turbulence structure and flux estimates by airborne measurements. *J. Geophys. Res. Atmos.*, **122**, 2115–2130, <https://doi.org/10.1002/2016JD025960>.
- Browning, K. A., D. J. Smart, M. R. Clark, and A. J. Illingworth, 2015: The role of evaporating showers in the transfer of sting-jet momentum to the surface. *Quart. J. Roy. Meteor. Soc.*, **141**, 2956–2971, <https://doi.org/10.1002/qj.2581>.
- Clark, P. A., and S. L. Gray, 2018: Sting jets in extratropical cyclones: a review. *Quart. J. Roy. Meteor. Soc.*, **144**, 943–969, <https://doi.org/10.1002/qj.3267>.
- Della-Marta, P. M., H. Mathis, C. Frei, M. A. Liniger, J. Klein, and C. Appenzeller, 2009: The return period of wind storms

- over Europe. *Int. J. Climatol.*, **29**, 437–459, <https://doi.org/10.1002/joc.1794>.
- Dipankar, A., B. Stevens, R. Heinze, C. Moseley, G. Zängl, M. Giorgetta, and S. Brdar, 2015: Large eddy simulation using the general circulation model icon. *J. Adv. Model. Earth Syst.*, **7** (3), 963–986, <https://doi.org/10.1002/2015MS000431>.
- Eberly, D., 2012: *Ridges in Image and Data Analysis*. Vol. 7. Springer Science & Business Media, 238 pp.
- Eisenstein, L., F. Pantillon, and P. Knippertz, 2019: Dynamics of sting-jet storm “Egon” over continental Europe: Impact of surface properties and model resolution. *Quart. J. Roy. Meteor. Soc.*, in press, <https://doi.org/10.1002/qj.3666>.
- Etling, D., and R. A. Brown, 1993: Roll vortices in the planetary boundary layer: A review. *Bound.-Layer Meteor.*, **65**, 215–248, <https://doi.org/10.1007/BF00705527>.
- Friederichs, P., M. Göber, S. Bentzien, A. Lenz, and R. Krampitz, 2009: A probabilistic analysis of wind gusts using extreme value statistics. *Meteor. Z.*, **18**, 615–629, <https://doi.org/10.1127/0941-2948/2009/0413>.
- Heinze, R., and Coauthors, 2017: Large-eddy simulations over Germany using ICON: A comprehensive evaluation. *Quart. J. Roy. Meteor. Soc.*, **143**, 69–100, <https://doi.org/10.1002/qj.2947>.
- Hewson, T. D., and U. Neu, 2015: Cyclones, windstorms and the IMILAST project. *Tellus*, **67A**, 27128, <https://doi.org/10.3402/tellusa.v67.27128>.
- Kalthoff, N., and Coauthors, 2013: KITcube—A mobile observation platform for convection studies deployed during HyMeX. *Meteor. Z.*, **22**, 633–647, <https://doi.org/10.1127/0941-2948/2013/0542>.
- Klawe, M., and U. Ulbrich, 2003: A model for the estimation of storm losses and the identification of severe winter storms in Germany. *Nat. Hazards Earth Syst. Sci.*, **3**, 725–732, <https://doi.org/10.5194/nhess-3-725-2003>.
- Kohler, M., J. Metzger, and N. Kalthoff, 2018: Trends in temperature and wind speed from 40 years of observations at a 200-m high meteorological tower in southwest Germany. *Int. J. Climatol.*, **38**, 23–34, <https://doi.org/10.1002/joc.5157>.
- Lamb, H. H., and K. Frydendahl, 1991: *Historic Storms of the North Sea, British Isles and Northwest Europe*. Cambridge University Press, 204 pp.
- Larsén, X. G., S. E. Larsen, and E. L. Petersen, 2016: Full-scale spectrum of boundary-layer winds. *Bound.-Layer Meteor.*, **159**, 349–371, <https://doi.org/10.1007/s10546-016-0129-x>.
- Lilly, D. K., 1962: On the numerical simulation of buoyant convection. *Tellus*, **14**, 148–172, <https://doi.org/10.3402/tellusa.v14i2.9537>.
- Lindeberg, T., 1998: Edge detection and ridge detection with automatic scale selection. *Int. J. Comput. Vis.*, **30**, 117–156, <https://doi.org/10.1023/A:1008097225773>.
- Ludwig, P., J. G. Pinto, S. A. Hoeppe, A. H. Fink, and S. L. Gray, 2015: Secondary cyclogenesis along an occluded front leading to damaging wind gusts: Windstorm Kyrill, January 2007. *Mon. Wea. Rev.*, **143**, 1417–1437, <https://doi.org/10.1175/MWR-D-14-00304.1>.
- Marke, T., S. Crewell, V. Schemann, J. H. Schween, and M. Tuononen, 2018: Long-term observations and high-resolution modeling of midlatitude nocturnal boundary layer processes connected to low-level jets. *J. Appl. Meteor. Climatol.*, **57**, 1155–1170, <https://doi.org/10.1175/JAMC-D-17-0341.1>.
- Muñoz Esparza, D., R. Sharman, J. Sauer, and B. Kosović, 2018: Toward low-level turbulence forecasting at eddy-resolving scales. *Geophys. Res. Lett.*, **45**, 8655–8664, <https://doi.org/10.1029/2018GL078642>.
- Neiman, P. J., R. M. Hardesty, M. A. Shapiro, and R. E. Cupp, 1988: Doppler lidar observations of a downslope windstorm. *Mon. Wea. Rev.*, **116**, 2265–2275, [https://doi.org/10.1175/1520-0493\(1988\)116<2265:DLOAD>2.0.CO;2](https://doi.org/10.1175/1520-0493(1988)116<2265:DLOAD>2.0.CO;2).
- Newsom, R., R. Calhoun, D. Ligon, and J. Allwine, 2008: Linearly organized turbulence structures observed over a suburban area by dual-Doppler lidar. *Bound.-Layer Meteor.*, **127**, 111–130, <https://doi.org/10.1007/s10546-007-9243-0>.
- Panofsky, H. A., H. Tennekes, D. H. Lenschow, and J. C. Wyngaard, 1977: The characteristics of turbulent velocity components in the surface layer under convective conditions. *Bound.-Layer Meteor.*, **11**, 355–361, <https://doi.org/10.1007/BF02186086>.
- Pantillon, F., S. Lerch, P. Knippertz, and U. Corsmeier, 2018a: Forecasting wind gusts in winter storms using a calibrated convection-permitting ensemble. *Quart. J. Roy. Meteor. Soc.*, **144**, 1864–1881, <https://doi.org/10.1002/qj.3380>.
- , A. Wieser, B. Adler, U. Corsmeier, and P. Knippertz, 2018b: Overview and first results of the Wind and Storms Experiment (WASTEX): A field campaign to observe the formation of gusts using a Doppler lidar. *Adv. Sci. Res.*, **15**, 91–97, <https://doi.org/10.5194/asr-15-91-2018>.
- Parton, G., A. Dore, and G. Vaughan, 2010: A climatology of mid-tropospheric mesoscale strong wind events as observed by the MST radar, Aberystwyth. *Meteor. Appl.*, **17**, 340–354, <https://doi.org/10.1002/met.203>.
- Peralta, C., Z. Ben Bouallégue, S. E. Theis, C. Gebhardt, and M. Buchhold, 2012: Accounting for initial condition uncertainties in COSMO-DE-EPS. *J. Geophys. Res.*, **117**, D07108, <https://doi.org/10.1029/2011JD016581>.
- Pinto, J. G., F. Pantillon, P. Ludwig, M.-S. Déroche, G. Leoncini, C. C. Raible, L. C. Shaffrey, and D. B. Stephenson, 2019: From atmospheric dynamics to insurance losses: An interdisciplinary workshop on European storms. *Bull. Amer. Meteor. Soc.*, **100**, ES175–ES178, <https://doi.org/10.1175/BAMS-D-19-0026.1>.
- Richner, H., and P. Hächler, 2013: Understanding and forecasting alpine foehn. *Mountain Weather Research and Forecasting: Recent Progress and Current Challenges*, F. K. Chow, S. F. J. De Wekker, and B. Snyder, Eds., Springer, 219–260.
- Roberts, J. F., and Coauthors, 2014: The XWS open access catalogue of extreme European windstorms from 1979 to 2012. *Nat. Hazards Earth Syst. Sci.*, **14**, 2487–2501, <https://doi.org/10.5194/nhess-14-2487-2014>.
- Rodriguez-Navarro, C., F. di Lorenzo, and K. Elert, 2018: Mineralogy and physicochemical features of Saharan dust wet deposited in the Iberian Peninsula during an extreme red rain event. *Atmos. Chem. Phys.*, **18**, 10 089–10 122, <https://doi.org/10.5194/acp-18-10089-2018>.
- Schultz, D. M., and Coauthors, 2018: Extratropical cyclones: A century of research on meteorology’s centerpiece. *A Century of Progress in Atmospheric and Related Sciences: Celebrating the American Meteorological Society Centennial*, *Meteor. Monogr.*, No. 59, 16.1–16.56, <https://doi.org/10.1175/AMSMONOGRAPHS-D-18-0015.1>.
- Schulz, J.-P., 2008: Revision of the turbulent gust diagnostics in the COSMO Model. *COSMO Newsletter*, No. 8, Consortium for Small-Scale Modeling, Offenbach, Germany, 17–22, http://www2.cosmo-model.org/content/model/documentation/newsLetters/newsLetter08/cnl8_schulz.pdf.
- Skamarock, W. C., 2004: Evaluating mesoscale NWP models using kinetic energy spectra. *Mon. Wea. Rev.*, **132**, 3019–3032, <https://doi.org/10.1175/MWR2830.1>.

- Stawiarski, C., K. Träumner, C. Kottmeier, C. Knigge, and S. Raasch, 2015: Assessment of surface-layer coherent structure detection in dual-Doppler lidar data based on virtual measurements. *Bound.-Layer Meteor.*, **156**, 371–393, <https://doi.org/10.1007/s10546-015-0039-3>.
- Suomi, I., and T. Vihma, 2018: Wind gust measurement techniques—From traditional anemometry to new possibilities. *Sensors*, **18**, 1300, <https://doi.org/10.3390/s18041300>.
- , S.-E. Gryning, E. J. O'Connor, and T. Vihma, 2017: Methodology for obtaining wind gusts using Doppler lidar. *Quart. J. Roy. Meteor. Soc.*, **143**, 2061–2072, <https://doi.org/10.1002/qj.3059>.
- Träumner, K., C. Kottmeier, U. Corsmeier, and A. Wieser, 2011: Convective boundary-layer entrainment: Short review and progress using Doppler lidar. *Bound.-Layer Meteor.*, **141**, 369–391, <https://doi.org/10.1007/s10546-011-9657-6>.
- , T. Damian, C. Stawiarski, and A. Wieser, 2015: Turbulent structures and coherence in the atmospheric surface layer. *Bound.-Layer Meteor.*, **154**, 1–25, <https://doi.org/10.1007/s10546-014-9967-6>.
- Young, G. S., D. A. R. Kristovich, M. R. Hjelmfelt, and R. C. Foster, 2002: Rolls, streets, waves, and more. *Bull. Amer. Meteor. Soc.*, **83**, 997–1002, <https://doi.org/10.1175/BAMS-83-7-Young>.
- Zängl, G., D. Reinert, P. Rípodas, and M. Baldauf, 2015: The ICON (icosahedral non-hydrostatic) modelling framework of DWD and MPI-M: Description of the non-hydrostatic dynamical core. *Quart. J. Roy. Meteor. Soc.*, **141**, 563–579, <https://doi.org/10.1002/qj.2378>.
- Zhou, K., N. Cherukuru, X. Sun, and R. Calhoun, 2018: Wind gust detection and impact prediction for wind turbines. *Remote Sens.*, **10**, 514, <https://doi.org/10.3390/rs10040514>.